Tissue Classification Based on 3D Local Intensity Structures for Volume Rendering

Yoshinobu Sato, *Member*, *IEEE*, Carl-Fredrik Westin, *Member*, *IEEE*, Abhir Bhalerao, Shin Nakajima, Nobuyuki Shiraga, Shinichi Tamura, *Member*, *IEEE*, and Ron Kikinis

Abstract—This paper describes a novel approach to tissue classification using three-dimensional (3D) derivative features in the volume rendering pipeline. In conventional tissue classification for a scalar volume, tissues of interest are characterized by an opacity transfer function defined as a one-dimensional (1D) function of the original volume intensity. To overcome the limitations inherent in conventional 1D opacity functions, we propose a tissue classification method that employs a multidimensional opacity function, which is a function of the 3D derivative features calculated from a scalar volume as well as the volume intensity. Tissues of interest are characterized by explicitly defined classification rules based on 3D filter responses highlighting local structures, such as edge, sheet, line, and blob, which typically correspond to tissue boundaries, cortices, vessels, and nodules, respectively, in medical volume data. The 3D local structure filters are formulated using the gradient vector and Hessian matrix of the volume intensity function combined with isotropic Gaussian blurring. These filter responses and the original intensity define a multidimensional feature space in which multichannel tissue classification strategies are designed. The usefulness of the proposed method is demonstrated by comparisons with conventional single-channel classification using both synthesized data and clinical data acquired with CT (computed tomography) and MRI (magnetic resonance imaging) scanners. The improvement in image quality obtained using multichannel classification is confirmed by evaluating the contrast and contrast-to-noise ratio in the resultant volume-rendered images with variable opacity values.

Index Terms—Volume visualization, image enhancement, medical image, 3D derivative feature, multiscale analysis, multidimensional opacity function, multichannel classification, partial volume effect.

1 Introduction

Volume rendering [1], [2] is a powerful visualization tool, especially useful in medical applications [3], [4] for which the basic requirement is the ability to visualize specific tissues of interest in relation to surrounding structures. Tissue classification is one of the most important processes in the volume rendering pipeline and, at present, it is commonly based on a histogram of intensity values in original volume data. Probabilistic and fuzzy classification have also been employed instead of binary classification in order to relate the probability of the existence of each tissue to opacity and color transfer functions [5]. Nevertheless, the performance of a classification method is largely limited by the quality of the feature measurements, however mathematically elaborate it is. Thus, one-dimensional (1D) opacity functions using only the original intensity as the feature measurement often suffer from inherent limitations in classifying voxels into tissues of interest and unwanted ones. Among the efforts that have been made to overcome this problem, one involves the use of multispectral information. In the medical field, vector-valued MR volume data acquired with different imaging protocols have been used for multichannel classifiers [6], [7].

In this paper, we propose a novel approach to tissue classification for volume rendering, a preliminary report of which can be found in [8]. The basic idea is to characterize each tissue based not only on its original intensity values, but also its local intensity structures [9], [10], [11], [12], [13]. For example, blood vessels, bone cortices, and nodules are characterized by line-like, sheet-like, and blob-like structures, respectively. We therefore design three-dimensional (3D) filters based on the gradient vector and Hessian matrix of the volume intensity function combined with isotropic Gaussian blurring to enhance these specific 3D local intensity structures, and use the filter outputs as multichannel information for tissue classification. The classification process in volume rendering can be viewed as one of assigning opacity and color to each voxel. In our approach, opacity and color are assigned using a multidimensional feature space whose axes correspond to the filtered values calculated from a scalar volume, as well as its original intensity values. That is, a multidimensional opacity function is used for tissue classification. Here, it should be noted that the multiple feature measurements are obtained not from vector-valued data, but from scalar data. Through visualization using different imaging

- *Y. Sato and S. Tamura are with the Division of Functional Diagnostic Imaging, Biomedical Research Center, Graduate School of Medicine, Osaka University, Room D11, 2-2 Yamada-oka, Suita, Osaka 565-0871, Japan. E-mail: {yoshi, tamuras}@image.med.osaka-u.ac.jp.*
- *C.F. Westin and R. Kikinis are with Harvard Medical School, Brigham and Womens Hospital, Department of Radiology, 75 Francis St., Boston, MA 02115. E-mail: {westin, kikinis}@bwh.harvard.edu.*
- *A. Bhalerao is with the Department of Computer Science, University of Warwick, Coventry CV4 7AL, UK. E-mail: Abhir.Bhalerao@dcs.warwick.ac.uk.*
- *S. Nakajima is with the Nakakawachi Medical Center of Acute Medicine, 3-4-13 Nishi-Iwata, Higashi-Osaka, Osaka 578-0947, Japan. E-mail: shin_n@mui.biglobe.ne.jp.*
- *N. Shiraga is with the Department of Diagnostic Radiology, Keio University School of Medicine, 35 Shinanomachi, Shinjuku-ku, Tokyo 160-8582, Japan. E-mail: shiraga@msn.com.*

Manuscript received 30 Sept. 1998; revised 8 Feb. 2000; accepted 7 Mar. 2000. For information on obtaining reprints of this article, please send e-mail to: tvcg@computer.org, and reference IEEECS Log Number 109325.

modalities and anatomical structures, we demonstrate that multidimensional opacity functions based on 3D local intensity structures can be highly effective for characterizing tissues and that the quality of the resultant volume-rendered images is significantly improved.

The organization of the paper is as follows: In Section 2, we characterize the novelty of our approach through a review of related work. In Section 3, we formulate 3D filters for the enhancement of specific local intensity structures with variable scales. In Section 4, we describe multichannel classifiers based on local intensity structures. In Section 5, we present experimental results using both synthesized volumes and real CT (computed tomography) and MR (magnetic resonance) data. In Section 6, we discuss the work and indicate the directions of future research.

2 Related Work

2.1 Multidimensional Opacity Function Using Derivative Features

The earliest mention of a multidimensional opacity function was by Levoy [1], who assigned opacity as a two-dimensional (2D) function of intensity and gradient magnitude in order to highlight sharp changes in volume data, that is, object surfaces. More recently, Kindlmann and Durkin analyzed a 3D histogram whose axes correspond to the original intensity, gradient magnitude, and second derivative along the gradient vector [14]. While their main emphasis is on the semiautomated generation of an opacity function based on inspection of the 3D histogram, they demonstrate that surfaces with different contrasts can be discriminated using opacity assignment by a 2D function of intensity and gradient magnitude. The differences between the work of Kindlmann and Durkin and ours can be summarized as follows:

- Although Kindlmann and Durkin only use gradient magnitude as an additional variable of an opacity function, we use several types of feature measurements based on first and second derivatives, including gradient magnitude and second-order structures such as sheet, line, and blob.
- Even if we consider only the use of gradient magnitude, our approach focuses on its utility for avoiding misclassification due to partial voluming, which Kindlmann and Durkin do not address.

2.2 Dealing with Partial Volume Effects

The problem of avoiding misclassification due to partial voluming is one of the main issues in tissue classification. Multichannel information obtained from *vector-valued* MR data was effectively used by Laidlaw et al. to resolve the problem [15]. Although we address the same problem, our approach is different in that we demonstrate the utility of multichannel information obtained from *scalar* data rather than *vector-valued* data.

2.3 Image Analysis for Extracting Local Intensity Structures

Feature extraction is one of main research topics in the image processing field. In the 2D domain, various filtering techniques have been developed to enhance specific types of features and a unified approach for classifying local intensity structures using the Hessian matrix and gradient vector of the intensity function has been proposed [16]. Although there have been relatively few studies in the 3D domain, successful results have been reported in the enhancement of line structures such as blood vessels [9], [10], planer structures such as narrow articular spaces [17], and blob structures such as nodules [18]. Among these reports, one unified framework is based on a 3×3 tensor representing local orientation [11], [12], [17], which can be used to guide adaptive filtering for orientation sensitive smoothing. Another framework is based on a 3×3 Hessian matrix [9], [10], [13], which is similar to the tensor model, but based on directional second derivatives. The possibility of using the Hessian for line and sheet detection in volume data was suggested by Koller et al. [13]. Further, a line measure based on the Hessian and its multiscale integration was formulated and intensively analyzed by Sato et al. [9], [10]. The approach described in this paper has two novel features as compared with these previous studies.

- The multiscale line measure is extended and generalized to different types of local intensity structures, including sheet and blob.
- A multidimensional feature space whose axes correspond to different types of local intensity structures, as well as the original intensity values, is used to characterize each tissue.

3 Multicale 3D Filters for Enhancement of Local Structures

We design 3D filters responding to specific 3D local structures such as edge, sheet, line, and blob. The derived filters are based on the gradient vector and the Hessian matrix of the intensity function combined with normalized Gaussian derivatives. The filter characteristics are analyzed using Gaussian local structure models. The formulation of this section is the generalization of a line measure [10] to different second-order structures.

3.1 Measures of Similarity to Local Structures

Let $f(\mathbf{x})$ be an intensity function of a volume, where $\mathbf{x} = (x, y, z)$. The second-order approximation of $f(\mathbf{x})$ around $\mathbf{x}_0$ is given by

$$f_{\mathrm{II}}(\mathbf{x}) = f(\mathbf{x}_0) + (\mathbf{x} - \mathbf{x}_0)^\top \nabla f_0 + \frac{1}{2}(\mathbf{x} - \mathbf{x}_0)^\top \nabla^2 f_0 (\mathbf{x} - \mathbf{x}_0), \tag{1}$$

where ∇f_0 and $\nabla^2 f_0$ denote the gradient vector and the Hessian matrix at $\mathbf{x}_0$, respectively. Thus, the second-order structures of local intensity variations around each point of a volume can be described by the original intensity, the gradient vector, and the Hessian matrix.

The gradient vector is defined as

$$\nabla f = (f_x, f_y, f_z), \tag{2}$$

where partial derivatives of volume $f(\mathbf{x})$ are represented as $f_x = \frac{\partial}{\partial x} f$, $f_y = \frac{\partial}{\partial y} f$, and $f_z = \frac{\partial}{\partial z} f$. Gradient magnitude is given by

TABLE 1
Basic Conditions for Each Local Structure and Representative Anatomical Structures

Local Structure	*Eigenvalue Condition*	*Decomposed Condition*	*Example(s)*
Sheet	$\lambda_3 \ll \lambda_2 \simeq \lambda_1 \simeq 0.$	$\lambda_3 \ll 0$ & $\lambda_3 \ll \lambda_2 \simeq 0$ & $\lambda_3 \ll \lambda_1 \simeq 0$	cortex
Line	$\lambda_3 \simeq \lambda_2 \ll \lambda_1 \simeq 0.$	$\lambda_3 \ll 0$ & $\lambda_3 \simeq \lambda_2$ & $\lambda_2 \ll \lambda_1 \simeq 0$	vessel, bronchus
Blob	$\lambda_3 \simeq \lambda_2 \simeq \lambda_1 \ll 0.$	$\lambda_3 \ll 0$ & $\lambda_3 \simeq \lambda_2$ & $\lambda_2 \simeq \lambda_1$	nodule

Each structure is assumed to be brighter than the surrounding region.

$$|\nabla f| = \sqrt{f_x^2 + f_y^2 + f_z^2}.$$

The gradient magnitude has been widely used as a measure of similarity to a 3D edge structure.

The Hessian matrix is given by

$$\nabla^2 f = \begin{bmatrix} f_{xx} & f_{xy} & f_{xz} \\ f_{yx} & f_{yy} & f_{yz} \\ f_{zx} & f_{zy} & f_{zz} \end{bmatrix}, \tag{3}$$

where partial second derivatives of $f(\mathbf{x})$ are represented as $f_{xx} = \frac{\partial^2}{\partial x^2} f$, $f_{yz} = \frac{\partial^2}{\partial y \partial z} f$, and so on. Let the eigenvalues of $\nabla^2 f$ be λ_1, λ_2, λ_3 ($\lambda_1 \geq \lambda_2 \geq \lambda_3$), and their corresponding eigenvectors be $\mathbf{e}_1$, $\mathbf{e}_2$, $\mathbf{e}_3$, respectively. The eigenvector $\mathbf{e}_1(\mathbf{x})$, corresponding to the largest eigenvalue $\lambda_1(\mathbf{x})$, represents the direction along which the second derivative is maximum, and $\lambda_1(\mathbf{x})$ gives the maximum second-derivative value. Similarly, $\lambda_3(\mathbf{x})$ and $\mathbf{e}_3(\mathbf{x})$ give the minimum directional second-derivative value and its direction, and $\lambda_2(\mathbf{x})$ and $\mathbf{e}_2(\mathbf{x})$ the minimum directional second-derivative value orthogonal to $\mathbf{e}_3(\mathbf{x})$ and its direction, respectively. $\lambda_2(\mathbf{x})$ and $\mathbf{e}_2(\mathbf{x})$ also give the maximum directional second-derivative value orthogonal to $\mathbf{e}_1(\mathbf{x})$ and its direction.

f, $|\nabla f|$, λ_1, λ_2, and λ_3 are invariant under orthonormal transformations. A multidimensional space can be defined whose axes correspond to these invariant measurements. The basic idea of the proposed method is to use the multidimensional space for tissue classification—by contrast, only f is usually used in the conventional method.

f and $|\nabla f|$ can be regarded as the intensity itself and the edge strength, respectively, which are intuitive feature measurements of local intensity structures. Thus, we define the $\mathcal{S}_{int}$ filter, which takes an original scalar volume f into a scalar volume of intensity, as

$$\mathcal{S}_{int}\{f\} = f, \tag{4}$$

and the $\mathcal{S}_{edge}$ filter, which takes an original scalar volume into a scalar volume of a measure of similarity to an edge, as

$$\mathcal{S}_{edge}\{f\} = |\nabla f|. \tag{5}$$

λ_1, λ_2, and λ_3 are combined and associated with the intuitive measures of similarity to local structures. Three types of second-order local structures—sheet, line, and blob—can be classified using these eigenvalues. The basic conditions of these local structures and examples of anatomical structures that they represent are summarized in Table 1, which shows the conditions for the case where structures are bright in contrast with surrounding regions. Conditions can be similarly specified for the case where the contrast is reversed. Based on these conditions, measures of similarity to these local structures can be derived. With respect to the case of a line, we have already proposed a line filter that takes an original volume f into a volume of a line measure [10] given by

$$\mathcal{S}_{line}\{f\} = \begin{cases} |\lambda_3| \cdot \psi(\lambda_2; \lambda_3) \cdot \omega(\lambda_1; \lambda_2) & \lambda_3 \leq \lambda_2 < 0 \\ 0, & \text{otherwise,} \end{cases} \tag{6}$$

where ψ is a weight function written as

$$\psi(\lambda_s; \lambda_t) = \begin{cases} (\frac{\lambda_s}{\lambda_t})^\gamma, & \lambda_t \leq \lambda_s < 0 \\ 0, & \text{otherwise,} \end{cases} \tag{7}$$

in which γ controls the sharpness of selectivity for the conditions of each local structure (Fig. 1a), and ω is written as

$$\omega(\lambda_s; \lambda_t) = \begin{cases} (1 + \frac{\lambda_s}{|\lambda_t|})^\gamma & \lambda_t \leq \lambda_s \leq 0 \\ (1 - \alpha \frac{\lambda_s}{|\lambda_t|})^\gamma & \frac{|\lambda_t|}{\alpha} > \lambda_s > 0 \\ 0, & \text{otherwise,} \end{cases} \tag{8}$$

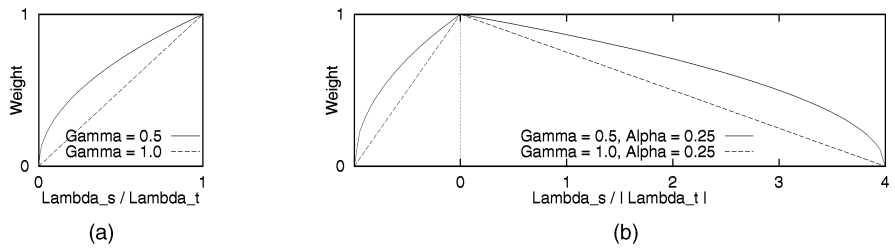

Fig. 1. Weight functions in measures of similarity to local structures. (a) $\psi(\lambda_s; \lambda_t)$, representing the condition $\lambda_t \simeq \lambda_s$, where $\lambda_t \leq \lambda_s$. $\psi(\lambda_s; \lambda_t) = 1$ when $\lambda_t = \lambda_s$. $\psi(\lambda_s; \lambda_t) = 0$ when $\lambda_s = 0$. (b) $\omega(\lambda_s; \lambda_t)$, representing the condition $\lambda_t \ll \lambda_s \simeq 0$. $\omega(\lambda_s; \lambda_t) = 1$ when $\lambda_s = 0$. $\omega(\lambda_s; \lambda_t) = 0$ when $\lambda_t = \lambda_s \ll 0$ or $\lambda_s (\geq \frac{|\lambda_t|}{\alpha}) \gg 0$.

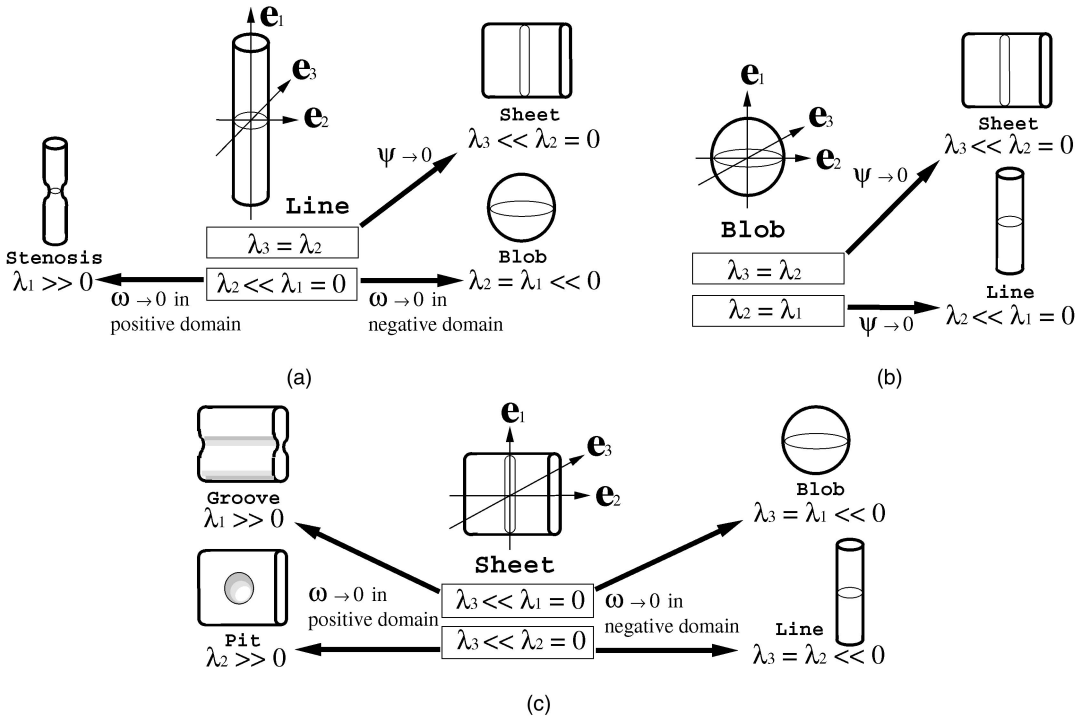

Fig. 2. Schematic diagrams of measures of similarity to local structures. The roles of weight functions in representing the basic conditions of a local structure are shown. (a) Line measure. The structure becomes sheet-like and the weight function ψ approaches zero with deviation from the condition $\lambda_3 \simeq \lambda_2$, blob-like and the weight function ω approaches zero with transition from the condition $\lambda_2 \ll \lambda_1 \simeq 0$ to $\lambda_2 \simeq \lambda_1 \ll 0$, and stenosis-like and the weight function ω approaches zero with transition from the condition $\lambda_2 \ll \lambda_1 \simeq 0$ to $\lambda_1 \gg 0$. (b) Blob measure. The structure becomes sheet-like with deviation from condition $\lambda_3 \simeq \lambda_2$, and line-like with deviation from the condition $\lambda_2 \simeq \lambda_1$. (c) Sheet measure. The structure becomes blob-like, groove-like, line-like, or pit-like with transition from $\lambda_3 \ll \lambda_1 \simeq 0$ to $\lambda_3 \simeq \lambda_1 \ll 0$, $\lambda_3 \ll \lambda_1 \simeq 0$ to $\lambda_1 \gg 0$, $\lambda_3 \ll \lambda_2 \simeq 0$ to $\lambda_3 \simeq \lambda_2 \ll 0$, or $\lambda_3 \ll \lambda_2 \simeq 0$ to $\lambda_2 \gg 0$, respectively.

in which $0 < \alpha \leq 1$ (Fig. 1b). α is introduced in order to give $\omega(\lambda_s; \lambda_t)$ an asymmetrical characteristic in the negative and positive regions of λ_s.

Fig. 2a shows the roles of weight functions in representing the basic conditions of the line case. In (6), $|\lambda_3|$ represents the condition $\lambda_3 \ll 0$, $\psi(\lambda_2; \lambda_3)$ represents the condition $\lambda_3 \simeq \lambda_2$ and decreases with deviation from the condition $\lambda_3 \simeq \lambda_2$, and $\omega(\lambda_1; \lambda_2)$ represents the condition $\lambda_2 \ll \lambda_1 \simeq 0$ and decreases with deviation from the condition $\lambda_1 \simeq 0$ which is normalized by λ_2. By multiplying $|\lambda_3|$, $\psi(\lambda_2; \lambda_3)$, and $\omega(\lambda_1; \lambda_2)$, we represent the condition for a line shown in Table 1. For the line case, the asymmetric characteristic of ω is based on the following observations:

- When λ_1 is negative, the local structure should be regarded as having a blob-like shape when $|\lambda_1|$ becomes large (lower right in Fig. 2a).
- When λ_1 is positive, the local structure should be regarded as being stenotic in shape (i.e., part of a vessel is narrowed), or it may be indicative of signal loss arising from the partial volume effect (lower left in Fig. 2a).

Therefore, when λ_1 is positive, we make the decrease with the deviation from the $\lambda_1 \simeq 0$ condition less sharp in order to still give a high response to a stenosis-like shape. We typically used $\alpha = 0.25$ and $\gamma = 0.5$ (or 1) in our experiments. Extensive analysis of the line measure, including the effects of parameters γ and α, can be found in [10].

The specific shape given in (7) is based on the need to generalize two line measures, $\sqrt{\lambda_3 \lambda_2}$ and $\min(-\lambda_3, -\lambda_2) = |\lambda_2|$ (where $\lambda_3 < \lambda_2 < 0$), suggested in earlier work [13]. These measures take into account the conditions $\lambda_3 \ll 0$ and $\lambda_3 \simeq \lambda_2$. $|\lambda_3| \cdot \psi(\lambda_2; \lambda_3)$ in (6) is equal to $\sqrt{\lambda_3 \lambda_2}$ and $|\lambda_2|$ when $\gamma = 0.5$ and $\gamma = 1$, respectively. In this formulation [10], the same type of function shape as that in (7) is used for (8) to add the condition $\lambda_2 \ll \lambda_1 \simeq 0$.

We can extend the line measure to the blob and sheet cases. In the blob case, the condition $\lambda_3 \simeq \lambda_2 \simeq \lambda_1 \ll 0$ can be decomposed into $\lambda_3 \ll 0$ and $\lambda_3 \simeq \lambda_2$ and $\lambda_2 \simeq \lambda_1$. By representing the condition $\lambda_t \simeq \lambda_s$ using $\psi(\lambda_s; \lambda_t)$, we can derive a blob filter given by

$$\mathcal{S}_{blob}\{f\} = \begin{cases} |\lambda_3| \cdot \psi(\lambda_2; \lambda_3) \cdot \psi(\lambda_1; \lambda_2) & \lambda_3 \leq \lambda_2 \leq \lambda_1 < 0 \\ 0, & \text{otherwise.} \end{cases} \tag{9}$$

In the sheet case, the condition $\lambda_3 \ll \lambda_2 \simeq \lambda_1 \simeq 0$ can be decomposed into $\lambda_3 \ll 0$ and $\lambda_3 \ll \lambda_2 \simeq 0$ and $\lambda_3 \ll \lambda_1 \simeq 0$. By representing the condition $\lambda_t \ll \lambda_s \simeq 0$ using $\omega(\lambda_s; \lambda_t)$, we can derive a sheet filter given by

$$\mathcal{S}_{sheet}\{f\} = \begin{cases} |\lambda_3| \cdot \omega(\lambda_2; \lambda_3) \cdot \omega(\lambda_1; \lambda_3) & \lambda_3 < 0 \\ 0, & \text{otherwise.} \end{cases} \tag{10}$$

Fig. 2b and Fig. 2c show the relationships between the eigenvalue conditions and weight functions in the blob and sheet measures.

3.2 Multiscale Computation and Integration of Filter Responses

Local structures can exist at various scales. For example, vessels and bone cortices can, respectively, be regarded as line and sheet structures with various widths. In order to make filter responses tunable to a width of interest, the derivative computation for the gradient vector and the Hessian matrix is combined with Gaussian convolution. By adjusting the standard deviation of Gaussian convolution, local structures with a specific range of widths can be enhanced. The Gaussian function is known as a unique distribution optimizing localization in both the spatial and frequency domains [19]. Thus, convolution operations can be applied within local support (due to spatial localization) with minimum aliasing errors (due to frequency localization).

We denote the local structure filtering for a volume blurred by Gaussian convolution with a standard deviation σ_f as

$$\mathcal{S}_\xi\{f;\sigma_f\}, \tag{11}$$

where $\xi \in \{int, edge, sheet, line, blob\}$. The filter responses decrease as σ_f in the Gaussian convolution increases unless appropriate normalization is performed [20], [21]. In order to determine the normalization factor, we consider a Gaussian-shaped model of edge, sheet, line, and blob with variable scales.

An ideal step edge is described as

$$h_{edge}(\mathbf{x}) = \begin{cases} 1, & \text{if } x > 0 \\ 0, & \text{otherwise,} \end{cases} \tag{12}$$

where $\mathbf{x} = (x, y, z)$. By combining Gaussian blur with (12), a blurred edge is modeled as

$$h_{edge}(\mathbf{x};\sigma_r) = \frac{1}{2\pi^{\frac{3}{2}}\sigma_r^3}\exp\left(-\frac{|\mathbf{x}|^2}{2\sigma_r^2}\right) * h_{edge}(\mathbf{x}), \tag{13}$$

where $*$ represents the convolution and σ_r is the standard deviation of the Gaussian function to control the degree of blurring.

Sheet, line, and blob structures with variable widths are modeled as

$$h_{sheet}(\mathbf{x};\sigma_r) = \exp\left(-\frac{x^2}{2\sigma_r^2}\right), \tag{14}$$

$$h_{line}(\mathbf{x};\sigma_r) = \exp\left(-\frac{x^2+y^2}{2\sigma_r^2}\right), \tag{15}$$

and

$$h_{blob}(\mathbf{x};\sigma_r) = \exp\left(-\frac{|\mathbf{x}|^2}{2\sigma_r^2}\right), \tag{16}$$

respectively, where σ_r controls the width of the structures.

We determine the normalization factor so that $\mathcal{S}_\xi\{h_\xi(\mathbf{x};\sigma_r);\sigma_f\}$ satisfies the following condition:

- $\max_{\sigma_r} \mathcal{S}_\xi\{h_\xi(\mathbf{0};\sigma_r);\sigma_f\}$ is constant, irrespective of σ_f, where $\mathbf{0} = (0,0,0)$.

The above condition can be satisfied when the Gaussian first and second derivatives are computed by multiplying by σ_f or σ_f^2, respectively, as the normalization factor. That is, the normalized Gaussian derivatives are given by

$$f_{x^p y^q}(\mathbf{x};\sigma_f) = \{\sigma_f^{p+q} \cdot \frac{\partial^{p+q}}{\partial x^p \partial y^q} G(\mathbf{x};\sigma_f)\} * f(\mathbf{x}), \tag{17}$$

where p and q are nonnegative integer values satisfying $p+q \le 2$, and $G(\mathbf{x};\sigma)$ is an isotropic 3D Gaussian function with a standard deviation σ (see Appendix A for the derivation of the normalization factor for second-order local structures). Fig. 3 shows the normalized response of $\mathcal{S}_\xi\{h_\xi(\mathbf{0};\sigma_r);\sigma_f\}$ (where $\sigma_f = \sigma_i s^{i-1}$, $\sigma_1 = 1$, $s = \sqrt{2}$, and $i = 1,2,3,4$) for $\xi \in \{edge, sheet, line, blob\}$ when σ_r is varied.

In the edge case, the maximum of the normalized response of $\mathcal{S}_{edge}\{h_{edge}(\mathbf{0},\sigma_r);\sigma_f\}$ is $\frac{1}{\sqrt{2\pi}}$ (≈ 0.399) when $\sigma_r = 0$, that is, the case of the ideal edge without blurring. By increasing σ_f, $\mathcal{S}_{edge}\{h_{edge}(\mathbf{0},\sigma_r);\sigma_f\}$ gives a higher response to blurred edges with a larger σ_r, while the response to the ideal edge remains constant (Fig. 3a).

In the line case, the maximum of the normalized response $\mathcal{S}_{line}\{h_{line}(\mathbf{0},\sigma_r);\sigma_f\}$ is $\frac{1}{4}(=0.25)$ when $\sigma_r = \sigma_f$ [10]. That is, $\mathcal{S}_{line}\{f;\sigma_f\}$ is regarded as being tuned to line structures with a width $\sigma_r = \sigma_f$. A line filter with a single scale gives a high response in only a narrow range of widths. We call the curves shown in Fig. 3b, Fig. 3c, and Fig. 3d *width response curves*, which represent filter characteristics like frequency response curves. The width response curve of the line filter can be adjusted and widened using multiscale integration of filter responses given by

$$\mathcal{M}_{line}\{f;\sigma_1,s,n\} = \max_{1\le i\le n} \mathcal{S}_{line}\{f;\sigma_i\}, \tag{18}$$

where $\sigma_i = s^{i-1}\sigma_1$, in which σ_1 is the smallest scale, s is a scale factor, and n is the number of scales [10]. The width response curve of multiscale integration using the four scales consists of the maximum values among the four single-scale width response curves and gives nearly uniform responses in the width range between $\sigma_r = \sigma_1$ and $\sigma_r = \sigma_4$ when $s = \sqrt{2}$ (Fig. 3b). While the width response curve can be perfectly uniform if continuous variation values are used for σ_f, the deviation from the continuous case is less than 3 percent using discrete values for σ_f with $s = \sqrt{2}$ [10]. Similarly, in the cases of $\mathcal{S}_{sheet}\{h_{sheet}(\mathbf{0},\sigma_r);\sigma_f\}$ and $\mathcal{S}_{blob}\{h_{blob}(\mathbf{0},\sigma_r);\sigma_f\}$, the maximum of the normalized response is $\frac{2}{(\sqrt{3})^3}(\approx 0.385)$ when $\sigma_r = \frac{\sigma_f}{\sqrt{2}}$ (Fig. 3c), and $\frac{2}{3}(\sqrt{\frac{3}{5}})^5(\approx 0.186)$ when $\sigma_r = \sqrt{\frac{3}{2}}\sigma_f$ (Fig. 3d), respectively (see Appendix A for the derivation of the above relationships). For the second-order cases, the width response curve can be adjusted and widened using the multiscale integration method given by

$$\mathcal{M}_{\xi_2}\{f;\sigma_1,s,n\} = \max_{1\le i\le n} \mathcal{S}_{\xi_2}\{f;\sigma_i\}, \tag{19}$$

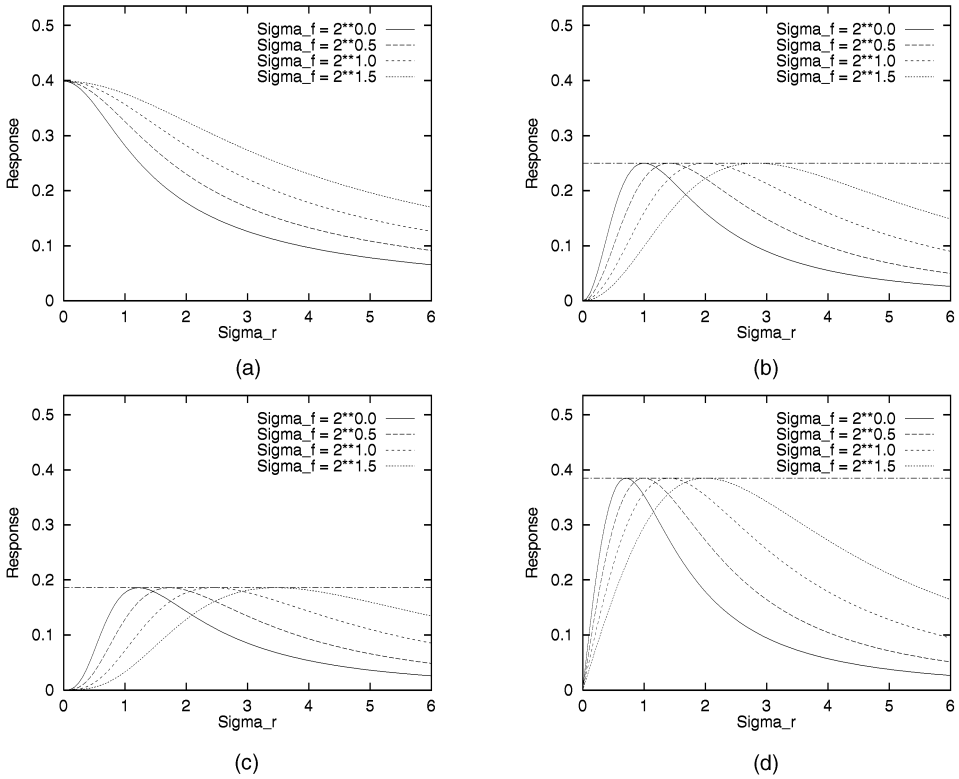

Fig. 3. Plots of normalized responses of local structure filters for corresponding local models, $\mathcal{S}_\xi\{h_\xi(\mathbf{0};\sigma_r);\sigma_f\}$, where σ_r is continuously varied and $\sigma_f = \sigma_i s^{i-1}$ ($\sigma_1 = 1$, $s = \sqrt{2}$, and $i = 1, 2, 3, 4$). See Appendix A for the theoretical derivations of the response curves shown in (b)-(d). (a) Response of the edge filter for the edge model ($\xi = edge$). (b) Response of the line filter for the line model ($\xi = line$). (c) Response of the blob filter for the blob model ($\xi = blob$). (d) Response of the sheet filter for the sheet model ($\xi = sheet$).

where $\xi_2 \in \{sheet, line, blob\}$.

$\mathcal{S}_{int}$ can also be extended so as to be combined with Gaussian blur, in which case we represent it as $\mathcal{S}_{int}\{f;\sigma_f\}$.

3.3 Implementation

Our 3D local structure filtering methods described above assume that volume data with isotropic voxels are used as input data. However, voxels in medical volume data are usually anisotropic since they generally have lower resolution along the third direction—i.e., the direction orthogonal to the slice plane—than within slices. Rotational invariant feature extraction becomes more intuitive in a space where the sample distances are uniform. That is, structures of a particular size can be detected on the same scale independent of the direction when the signal sampling is isotropic. We therefore introduce a preprocessing procedure for 3D local structure filtering in which we perform interpolation to make each voxel isotropic. Linear and spline-based interpolation methods are often used, but blurring is inherently involved in these approaches. Because, as noted above, the original volume data is inherently blurrier in the third direction, further degradation of the data in that direction should be avoided. For this reason, we opted to employ sinc interpolation so as not to introduce any additional blurring. After Gaussian-shaped slopes are added at the beginning and end of each profile in the third direction to avoid unwanted Gibbs ringing (see Appendix B), sinc interpolation is performed by zero-filled expansion in the frequency domain [22], [23].

The sinc interpolation and 3D local structure filtering were implemented on a Sun Enterprise server with multi-CPUs using multithreaded programming. With eight CPUs (168 MHz), interpolation and single-scale 3D filtering for a 256 × 256 × 128 volume were performed in about five minutes. Separable implementation was used for efficient 3D Gaussian derivative convolution. For example, the computation of the second derivatives of Gaussian in the Hessian matrix was implemented using three separate convolutions with one-dimensional kernels as represented by

$$f_{x^i y^j z^k}(\mathbf{x};\sigma_f) = \left\{\frac{\partial^2}{\partial x^i \partial y^j \partial z^k} G(\mathbf{x};\sigma_f)\right\} * f(\mathbf{x})$$
$$= \frac{d^i}{dx^i} G(x;\sigma_f) * \left\{\frac{d^j}{dy^j} G(y;\sigma_f) * \left\{\frac{d^k}{dz^k} G(z;\sigma_f) * f(\mathbf{x})\right\}\right\}, \quad (20)$$

where i, j, and k are nonnegative integers satisfying $i + j + k = 2$ and $4 \cdot \sigma_f$ was used as the radius of the kernel [10]. Using this decomposition, the amount of computation needed can be reduced from $O(n^3)$ to $O(3n)$, where n is the kernel diameter. Details of the implementation of eigenvalue computation for the Hessian matrix are described in [10].

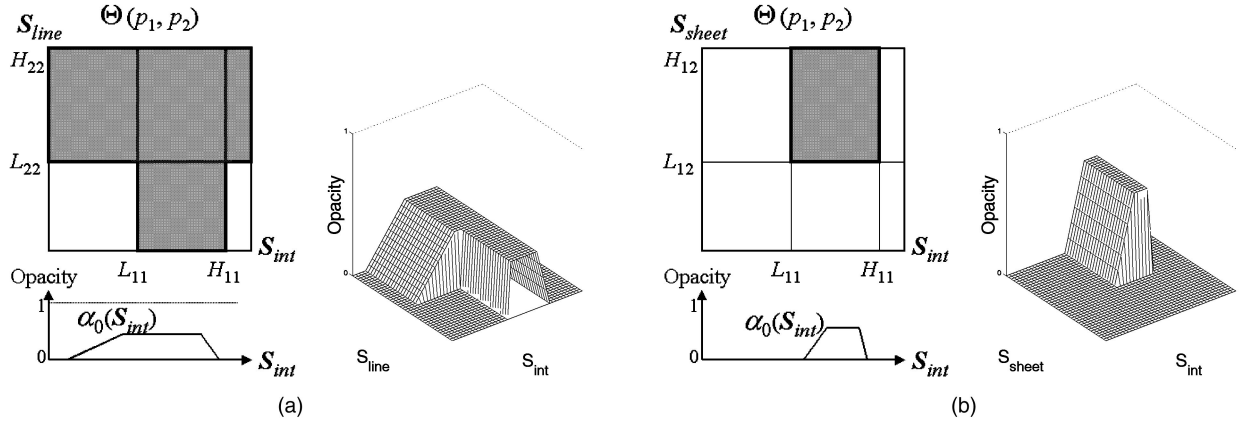

Fig. 4. Multichannel tissue classification. (a) Example using the max (OR) operations. Discrete classification $\Theta(\mathbf{p})$ (upper left) is obtained by combining $\theta(p_i)$ in different channels using the max (OR) operation. The resultant multidimensional opacity function $\alpha(\mathbf{p})$ (right) is obtained by the min of the discrete classification and a continuous one-dimensional (1D) opacity function $\alpha_0(\mathcal{S}_{int})$ (lower left). (b) Example using the min (AND)

4 Multichannel Tissue Classification Based on Local Structures

4.1 Representation of Classification Strategy

A multidimensional feature space can be defined whose axes correspond to the measures of similarity to different local structures selected from $\mathcal{S}_{\xi_{0,1}}$, $\mathcal{S}_{\xi_2}$, and $\mathcal{M}_{\xi_2}$, where $\xi_{0,1} \in \{int, edge\}$ and $\xi_2 \in \{sheet, line, blob\}$. Let $\mathbf{p} = (p_1, p_2, \ldots, p_m)$ (m is the number of features) be a feature vector in the multidimensional feature space, which consists of multichannel values of the measures of similarity to different local structures at each voxel. The opacity function $\alpha(\mathbf{p})$ and color function $\mathbf{c}(\mathbf{p}) = (R(\mathbf{p}), G(\mathbf{p}), B(\mathbf{p}))$ for volume rendering are given as functions of the multidimensional variable $\mathbf{p}$.

We consider the following problem: Given tissue classes $\mathbf{t} = (t_1, t_2, \ldots, t_n)$ (n is the number of tissue classes), how can we determine the tissue opacity function $\alpha_j(\mathbf{p})$ and tissue color $\mathbf{c}_j(\mathbf{p})$ for tissue t_j? We use a 1D weight function $\phi(p_i)$, whose range is $[0, 1]$, of feature p_i as a primitive function to specify the opacity function $\alpha_j(\mathbf{p})$ for tissue t_j. We consider a generalized combination rule of the 1D weight functions to obtain the opacity function $\alpha(\mathbf{p})$ formally given by

$$\alpha(\mathbf{p}) = \max\left\{\min_{1\le i\le m} \phi_{1,i}(p_i), \min_{1\le i\le m} \phi_{2,i}(p_i), \ldots, \min_{1\le i\le m} \phi_{ri}(p_i)\right\}, \tag{21}$$

where r is the number of terms $\min_{1\le i\le m} \phi_{ki}(p_i)$ and $\phi_{ki}(p_i)$ denotes the weight function for feature p_i in the kth term.

The max and min operations in (21) respectively correspond to union and intersection operations in fuzzy theory [24]. Suppose $\phi_{ki}(p_i)$ has a box-shaped function given by

$$\phi_{ki}(p_i) = \theta(p_i; L_{ki}, H_{ki}), \tag{22}$$

where

$$\theta(x; L, H) = \begin{cases} 1, & L \le x < H \\ 0, & \text{otherwise.} \end{cases} \tag{23}$$

When the opacity function of a 2D feature vector $\mathbf{p} = (p_1, p_2)$ is specified by

$$\begin{aligned} \alpha(\mathbf{p}) &= \max\{\min\{\theta(p_1; L_{11}, H_{11}), \theta(p_2; -\infty, \infty)\}, \\ &\qquad \min\{\theta(p_1; -\infty, \infty), \theta(p_2; L_{22}, H_{22})\}\} \\ &= \max\{\theta(p_1; L_{11}, H_{11}), \theta(p_2; L_{22}, H_{22})\}, \end{aligned} \tag{24}$$

where $\phi_{ki}(p_i) = \theta(p_i; L_{ki}, H_{ki})$, $r = 2$, $L_{12} = L_{21} = -\infty$, and $H_{12} = H_{21} = \infty$ in (21), the classification strategy can be viewed as:

$$\begin{aligned} &\text{IF} \quad L_{11} \le p_1 < H_{11} \ \text{ OR } \ L_{22} \le p_2 < H_{22} \\ &\text{THEN} \quad \alpha(\mathbf{p}) = 1 \quad \text{ELSE} \quad \alpha(\mathbf{p}) = 0. \end{aligned}$$

When the opacity function is specified by

$$\begin{aligned} \alpha(\mathbf{p}) &= \max\{\min\{\theta(p_1; L_{11}, H_{11}), \theta(p_2; L_{12}, H_{12})\}\} \\ &= \min\{\theta(p_1; L_{11}, H_{11}), \theta(p_2; L_{12}, H_{12})\}, \end{aligned} \tag{25}$$

where $r = 1$ in (21), the classification strategy can be viewed as:

$$\begin{aligned} &\text{IF} \quad L_{11} \le p_1 < H_{11} \quad \text{AND } \ L_{12} \le p_2 < H_{12} \\ &\text{THEN} \quad \alpha(\mathbf{p}) = 1 \qquad \text{ELSE} \quad \alpha(\mathbf{p}) = 0. \end{aligned}$$

By replacing $\theta(p_i; L_{ki}, H_{ki})$ with continuous weight functions, fuzzy operations can be incorporated into the classification strategy.

In practice, we chose the specific form of the opacity functions given by

$$\alpha(\mathbf{p}) = \min\{\alpha_0(\mathcal{S}_{int}), \Theta(\mathbf{p})\}, \tag{26}$$

where $\alpha_0(\mathcal{S}_{int})$ is a 1D weight function whose range is $[0, 1]$, and

$$\Theta(\mathbf{p}) = \max\left\{\min_{1\le i\le m} \theta_{1,i}(p_i; L_{1,i}, H_{1,i}), \ldots, \min_{1\le i\le m} \theta_{ri}(p_i; L_{ri}, H_{ri})\right\}. \tag{27}$$

Examples are shown in Fig. 4. It is easily verified by applying distributive laws that (26) is a special case of (21). When $\Theta(\mathbf{p}) = 1$, (26) is equivalent to the conventional tissue

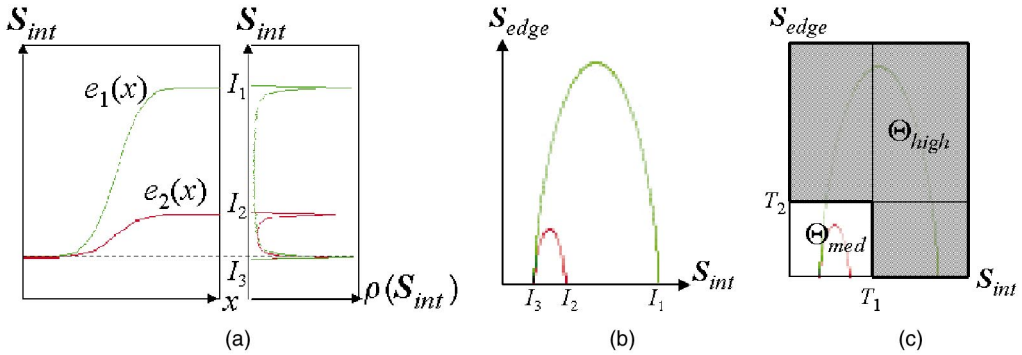

Fig. 5. Guideline 1: Using gradient magnitude to avoid misclassification due to partial voluming. (a) Profiles and 1D histograms $\rho(\mathcal{S}_{int})$ for edge models $e_1(\mathbf{x})$ (green plots) and $e_2(\mathbf{x})$ (red plots). (b) 2D histograms $\rho(\mathbf{p})$ for the two edge models where $\mathbf{p} = (\mathcal{S}_{int}, \mathcal{S}_{edge})$. The density of each plot corresponds to the value of $\rho(\mathbf{p})$. The 2D histogram distribution of each edge profile has an arch-shape. In order to keep the same relative relation of $\mathcal{S}_{int}$ and $\mathcal{S}_{\xi}$ (or $\mathcal{M}_{\xi}$), all of the 2D histograms shown in this paper were plotted within the domain described as $(\mathcal{S}_{int}, \mathcal{S}_{\xi}) \in [a, b] \times [0, 4(b-a)/15]$, where $[a, b]$ depends on each application. (c) Typical discrete classifications $\Theta_{high}(\mathbf{p})$ for $e_1(\mathbf{x})$ and $\Theta_{med}(\mathbf{p})$ for $e_2(\mathbf{x})$ to avoid misclassification due to partial voluming. T_2 should be selected based on the arch-shaped distribution observed in the 2D histogram $\rho(\mathcal{S}_{int}, \mathcal{S}_{edge})$ so that, as far as possible, Θ_{med} does not include voxels affected by the partial volume effect (green arch).

classification method solely based on the original intensity $\mathcal{S}_{int}$. The specific form given in (26) allows a simple design for the basic classification strategy, $\Theta(\mathbf{p})$, based on logic operations, while it creates the effects inherent in volume rendering by interactive adjustment of $\alpha_0(\mathcal{S}_{int})$ with continuous values. Furthermore, this form is suitable for implementation using conventional volume rendering software packages or hardware renderers (see Section 4.3 for a detailed description). Similarly, the color function $\mathbf{c}(\mathbf{p}) = (R(\mathbf{p}), G(\mathbf{p}), B(\mathbf{p}))$ is specified by

$$\begin{aligned}&(R(\mathbf{p}), G(\mathbf{p}), B(\mathbf{p})) = \\ &(\min\{r_0(\mathcal{S}_{int}), \Theta(\mathbf{p})\}, \min\{g_0(\mathcal{S}_{int}), \Theta(\mathbf{p})\}, \\ &\min\{b_0(\mathcal{S}_{int}), \Theta(\mathbf{p})\}),\end{aligned} \tag{28}$$

where $r_0(\mathcal{S}_{int})$, $g_0(\mathcal{S}_{int})$, and $b_0(\mathcal{S}_{int})$ are 1D color functions whose range is $[0, 1]$.

In summary, the processes of tissue classification and visualization consist of the following steps:

1. Define tissue classes $\mathbf{t} = (t_1, t_2, \ldots, t_n)$.
2. Design a classification strategy.
   a. Find the local structures to characterize each tissue class t_j $(j = 1, 2, \ldots, n)$ and determine the filter types and widths to define the multidimensional feature vector $\mathbf{p} = (p_1, p_2, \ldots, p_m)$.
   b. Determine $\Theta_j(\mathbf{p})$, defining the discrete classification for each tissue class t_j.
3. Interactively adjust the opacity $\alpha_j(\mathcal{S}_{int})$ and color $\mathbf{c}_j(\mathcal{S}_{int})$ for each tissue t_j to obtain desirable visualizations.

The first step is the process of problem definition based on the requirements of users such as clinicians and medical researchers. The second step includes the analysis of the problem and the design of the multichannel classifier and is performed by the designer. Guidelines for designing a classification strategy based on local structures are given below. The third step is the interactive process of parameter adjustment by the user.

4.2 Guidelines for Choosing Suitable Local Structures for Classification

4.2.1 Guideline 1: Using Gradient Magnitude to Avoid Misclassification Due to Partial Voluming

We consider two edge models, $e_1(\mathbf{x}) = (I_1 - I_3)h_{edge}(\mathbf{x}; \sigma_r) + I_3$ and $e_2(\mathbf{x}) = (I_2 - I_3)h_{edge}(\mathbf{x}; \sigma_r) + I_3$ (where $I_1 > I_2 > I_3$) based on (13) (Fig. 5a). We assume that I_1, I_2, and I_3 correspond to the average intensity values of tissue classes, t_1 ("high"-intensity tissue), t_2 ("medium"-intensity tissue), and t_3 ("low"-intensity background), respectively. Even if the intensity distributions (histograms) of these tissues are well-separated, ambiguous intensity values can exist at the boundaries between two different tissue regions due to the partial volume effect. Fig. 5a shows the histograms $\rho(\mathcal{S}_{int})$ for these edge models. If the two edges exist in the same volume data, misclassification occurs around I_2 when using the original intensity $\mathcal{S}_{int}$ only. Fig. 5b shows histograms plotted in a 2D feature space whose axes are $\mathcal{S}_{int}$ and $\mathcal{S}_{edge}$. The 2D histograms $\rho(\mathcal{S}_{int}, \mathcal{S}_{edge})$ are arch-shaped because intermediate intensity values occur at the boundaries where the gradient magnitude $\mathcal{S}_{edge}$ is high. When the arm of the arch reaches $\mathcal{S}_{edge} = 0$, $\mathcal{S}_{int}$ corresponds to the average intensity value of each tissue class. The intermediate intensities with high gradient magnitudes are distributed near the apex of the arch.

Based on the above observations, the feature vector $\mathbf{p} = (\mathcal{S}_{int}, \mathcal{S}_{edge})$ can be utilized to classify the voxels into two tissue classes, $\mathbf{t} =$ ("high", "medium"), without misclassification around $\mathcal{S}_{int} = I_2$. Fig. 5c illustrates the discrete classifications for this purpose. One of the typical opacity functions for tissue "med," $\alpha_{med}(\mathbf{p})$, is specified as

$$\begin{aligned}\alpha_{med}(\mathbf{p}) &= \min\{A_{med} \cdot \theta(\mathcal{S}_{int}; L_m, H_m), \Theta_{med}(\mathbf{p})\}, \\ \Theta_{med}(\mathbf{p}) &= \min\{\theta(\mathcal{S}_{int}; 0, T_1), \theta(\mathcal{S}_{edge}; 0, T_2)\},\end{aligned} \tag{29}$$

where A_{med} is the opacity value for tissue "med." $\alpha_{high}(\mathbf{p})$ for tissue "high" is specified as

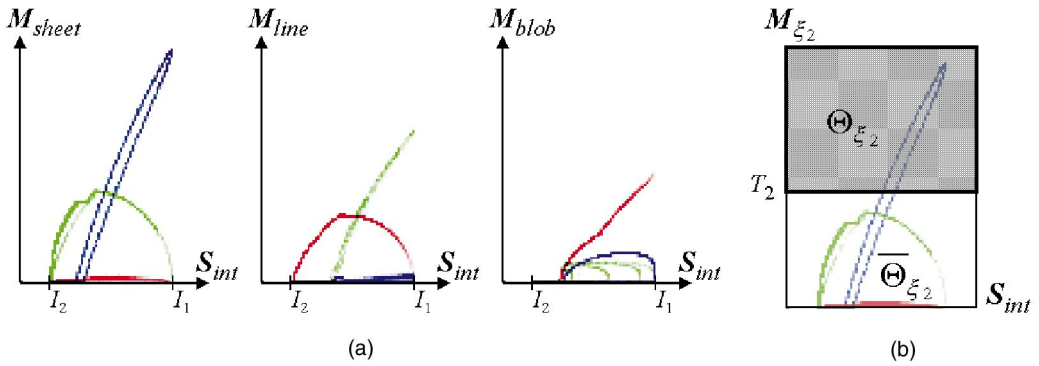

Fig. 6. Guideline 2: Using second-order local structures. (a) 2D histograms $\rho(\mathbf{p})$ for sheet (blue plots), line (green plots), and blob (red plots) models, where $\mathbf{p} = (\mathcal{S}_{int}, \mathcal{M}_{\xi_2})$ $(\xi_2 \in \{sheet, line, blob\})$. For the multiscale filter $\mathcal{M}_{\xi_2}$, $\sigma_1 = 1.0$, $s = \sqrt{2}$, $n = 4$ in (19). For the local structure model $h'_{\xi_2}(\mathbf{x}; \sigma_r), \sigma_r = 2.0$. The sheet and line models had spherical and circular shapes, respectively, whose radii were 64. The unit is voxels. Left: $\mathbf{p} = (\mathcal{S}_{int}, \mathcal{M}_{sheet})$. Middle: $\mathbf{p} = (\mathcal{S}_{int}, \mathcal{M}_{line})$. Right: $\mathbf{p} = (\mathcal{S}_{int}, \mathcal{M}_{blob})$. (b) Typical discrete classification $\Theta_{\xi_2}(\mathbf{p})$ for classifying each second-order structure. T_2 should be selected so that unwanted structures are removed while the target second-order structures are extracted.

$$\begin{aligned} \alpha_{high}(\mathbf{p}) &= \min\{A_{high} \cdot \theta(\mathcal{S}_{int}; L_h, H_h), \Theta_{high}(\mathbf{p})\}, \\ \Theta_{high}(\mathbf{p}) &= \bar{\Theta}_{med}(\mathbf{p}) \\ &= \max\{\theta(\mathcal{S}_{int}; T_1, \infty), \theta(\mathcal{S}_{edge}; T_2, \infty)\}, \end{aligned} \tag{30}$$

where $\bar{\Theta}_{med}(\mathbf{p}) = 1 - \Theta_{med}(\mathbf{p})$ and A_{high} is the opacity value for tissue "medium." These discrete classifications can be viewed as:

$$\begin{aligned} &\text{IF} \quad \mathcal{S}_{int} \text{ is low AND } \mathcal{S}_{edge} \text{ is low} \\ &\text{THEN} \quad \Theta_{med}(\mathbf{p}) = 1 \quad \text{ELSE} \quad \Theta_{high}(\mathbf{p}) = 1. \end{aligned}$$

Using the above classification strategy, voxels not affected by the partial volume effect can be separated from those so affected.

4.2.2 Guideline 2: Using Second-Order Local Structures

We consider the second-order local structure model $h'_{\xi_2}(\mathbf{x}) = (I_1 - I_2)h_{\xi_2}(\mathbf{x}; \sigma_r) + I_2$, (where

$$4\xi_2 \in \{sheet, line, blob\}$$

and $I_1 > I_2$) based on (14), (15), and (16). The classification of $h'_{sheet}(\mathbf{x})$ $h'_{line}(\mathbf{x})$, and $h'_{blob}(\mathbf{x})$ is inherently ambiguous using the original intensity $\mathcal{S}_{int}$ only. Fig. 6a shows histograms for sheet, line, and blob plotted in a 2D feature space whose axes are $\mathcal{S}_{int}$ and $\mathcal{M}_{\xi_2}$.

Based on the histograms, the feature vector $\mathbf{p} = (\mathcal{S}_{int}, \mathcal{M}_{\xi_2})$ (or $(\mathcal{S}_{int}, \mathcal{S}_{\xi_2})$) can be utilized to classify the voxels into two tissue classes, $\mathbf{t} = (\xi_2, \bar{\xi}_2)$, where $\bar{\xi}_2$ represents all other structures different from ξ_2. Fig. 6b illustrates the discrete classifications for this purpose. The discrete classifications $\Theta_{\xi_2}(\mathbf{p})$ and $\Theta_{\bar{\xi}_2}(\mathbf{p})$ are specified as

$$\Theta_{\xi_2}(\mathbf{p}) = \theta(\mathcal{M}_{\xi_2}; T_2, \infty), \tag{31}$$

and

$$\Theta_{\bar{\xi}_2}(\mathbf{p}) = \bar{\Theta}_{\xi_2}(\mathbf{p}) = \theta(\mathcal{M}_{\xi_2}; 0, T_2). \tag{32}$$

These discrete classifications can be viewed as:

$$\text{IF} \quad \mathcal{M}_{\xi_2} \text{ is high} \quad \text{THEN} \quad \Theta_{\xi_2}(\mathbf{p}) = 1 \quad \text{ELSE} \quad \Theta_{\bar{\xi}_2}(\mathbf{p}) = 1.$$

Using the above classification strategy, voxels with similar intensity values can be classified into ξ_2 structures and others. Selecting a filter of the type ξ_2 is a simple process. This filter type directly corresponds to the local structure of a tissue to be highlighted or suppressed, as shown in Table 1. The filter width and its multiscale integration can be determined according to the width response curves shown in Fig. 3 if the actual width range of a target tissue can be found.

4.2.3 Summary of Guidelines

The two procedures outlined above for improved tissue classification using 3D local structures can be summarized as follows:

Guideline 1 (dealing with the partial volume effect): At the boundaries of tissues, intermediate intensity values often exist that are not inherent to the tissues themselves. When a tissue of interest has intensity values similar to such intermediate values, misclassification occurs. Discrete classification $\Theta_{med}(\mathbf{p})$ in a 2D feature space $(\mathcal{S}_{int}, \mathcal{S}_{edge})$ is a useful means of avoiding such misclassification.

Guideline 2 (discriminating second-order features): When a tissue of interest can be characterized by its line, sheet, or blob structure, as well as its intensity values, discrete classification $\Theta_{\xi_2}(\mathbf{p})$ in a 2D feature space $(\mathcal{S}_{int}, \mathcal{M}_{\xi_2})$ (where $\xi_2 \in \{sheet, line, blob\}$) is a useful means of improving the classification.

Classification strategies are designed based on an interactive analysis of the local intensity structure of each tissue class by repeating the following processes. First, unwanted tissues that could be confused with the target tissue when only the original intensity is used are identified Second, a 3D local structure filter expected to be effective in disambiguating these tissues is selected based on the above two guidelines. Finally, the discrete classification based on a 2D histogram analysis is determined and then checked to see whether the disambiguation power is sufficiently improved when the 2D feature space defined by the original intensity and the filter response is used. The above procedures are repeated for the remaining tissues until the classification of all the tissues becomes satisfactory. Since discrete classification can be viewed as an IF–THEN–ELSE rule, its sequential application represents a nested set of the IF–THEN–ELSE rules.

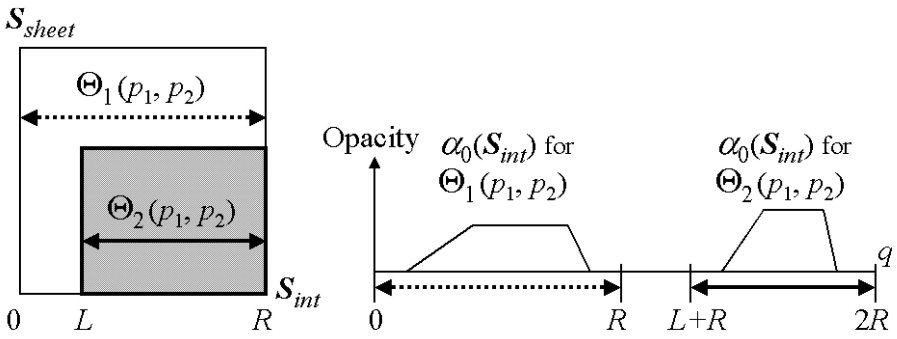

Fig. 7. Implementations of multichannel tissue classification on a conventional single-channel classifier. Voxels classified by Θ_1 and Θ_2 (left) are assigned to $[0, R)$ and $[L + R, 2R)$ (right), respectively (see text).

4.3 Implementation

From the practical aspect, one problem to be addressed is the implementation of the multichannel tissue classification method using software packages [25], [26] or hardware volume renderers intended for conventional volume rendering. We implemented the method using the volume rendering modules in the Visualization Toolkit (vtk, version 2.0) [25]. These vtk modules generate both unshaded and shaded composite images from a scalar volume (in our all experiments, unshaded composite images were generated). To deal with a vector-valued volume for multichannel tissue classification, we convert a vector-valued volume to a scalar volume using the discrete classification $\Theta_j(\mathbf{p})$ (27) for each tissue class t_j ($j = 1, \ldots, n$), where we assume $\min\{\Theta_j(\mathbf{p}), \Theta_k(\mathbf{p})\} = 0$ ($j \neq k$). We assign to each voxel the scalar value q, uniquely determined by its intensity value $\mathcal{S}_{int}$ and tissue class t_j given by $\Theta_j(\mathbf{p})$. If it can be assumed that $p_i \in [0, R)$, one possible form of q is $q(j, \mathcal{S}_{int}) = \mathcal{S}_{int} + (j - 1) \cdot R$. The full range assigned to a scalar value of each voxel, which is 16 bits in the vtk, is divided into subrange segments with length R and the segmented range of the interval $[(j - 1) \cdot R,\ j \cdot R)$ is used to represent the intensity value $\mathcal{S}_{int}$ for the tissue class t_j. Thus, $\alpha_j(\mathcal{S}_{int})$ and $\mathbf{c}_j(\mathcal{S}_{int})$ for each tissue class t_j are shifted to $\alpha(q(j, \mathcal{S}_{int}))$ and $\mathbf{c}(q(j, \mathcal{S}_{int}))$, where $q(j, \mathcal{S}_{int}) \in [(j - 1) \cdot R,\ j \cdot R)$. Fig. 7 shows an example of classification using $p_1 = \mathcal{S}_{int}$ and $p_2 = \mathcal{S}_{sheet}$. Voxels are classified into tissue classes t_1 and t_2 using $\Theta_1(p_1, p_2)$ and $\Theta_2(p_1, p_2)$, respectively (Fig. 7, left). For the voxels classified using $\Theta_1(p_1, p_2)$ (i.e., $j = 1$), their intensity values $\mathcal{S}_{int}$ are converted by $q(j, \mathcal{S}_{int}) = \mathcal{S}_{int} + (j - 1) \cdot R = \mathcal{S}_{int}$. Similarly, for the voxels classified using $\Theta_2(p_1, p_2)$ (i.e., $j = 2$), $q(j, \mathcal{S}_{int}) = \mathcal{S}_{int} + R$. The segmented ranges of the interval $[0, R)$ and $[R, 2R)$ are assigned to voxels with t_1 and t_2, respectively. Since $\mathcal{S}_{int} \geq L$ with respect to voxels with t_2 in Fig. 7, the interval substantially becomes $[L + R, 2R)$ (Fig. 7, right).

5 Experimental Results

5.1 Simulation Using Synthesized Images

Simulation experiments were performed to show how local intensity structures can be used to improve the performance of tissue classification. Typical situations in medical volume data were modeled by synthesized images. The contrast and contrast-to-noise ratio were used as measures to quantify the improvement.

5.1.1 Avoiding Misclassification Due to Partial Voluming

We assumed that three tissue classes, t_1, t_2, and t_3, existed in the volume data. Let I_1, I_2, and I_3 be the average intensity values of t_1, t_2, and t_3, respectively, and suppose $I_1 > I_2 > I_3$. We modeled a situation where a "medium"-intensity tissue (t_2), which was assumed to be the target tissue, was surrounded by a "high"-intensity tissue (t_1) on a "low"-intensity background (t_3). Fig. 8a shows a cross section of the synthesized volume with random noise (where $I_1 \approx 100$, $I_2 \approx 25$, and $I_3 \approx 0$), and Fig. 8b depicts a volume-rendered image of the synthesized volume viewed from an oblique direction. A thin rectangle of medium intensity (whose profile was a Gaussian function with a height and standard deviation of 25 and 1.0, respectively) was surrounded by an oval-shaped wall of high intensity (whose profile was a Gaussian function with a height and standard deviation of 100 and 3.0, respectively). The goal was to visualize the target tissue t_2 through the surrounding tissue t_1 without the effect of partial voluming, that is, the intrusion of unwanted intermediate intensities between the surrounding tissue t_1 and the background t_3.

Guideline 1 was utilized to classify the voxels into two tissue classes, $\mathbf{t} =$ ("high," "medium") using the feature vector $\mathbf{p} = (\mathcal{S}_{int}, \mathcal{S}_{edge})$, where $\sigma_f = 1.0$ in (11) for $\mathcal{S}_{edge}$. (Hereafter, the unit is voxels if not specified.) Fig. 8c shows rendered images obtained using multichannel classification. The images in the left and middle frames, rendered with two different opacities, were intended to visualize only the target tissue "medium." In these images, the contrast of the target tissue was sufficiently high since the effect of overlapping unwanted intensities was mostly removed due to their high gradient magnitude. The right frame is a color-rendered image of the "high"- (white) and "medium"- (pink) intensity regions. In this case, both structures were clearly depicted by the different colors. Fig. 8d shows rendered images obtained using single-channel classification based on the original intensity, $\mathcal{S}_{int}$. In the left and middle frames, the target tissue was only vaguely imaged due to unwanted intermediate intensities. In the color-rendered image (right frame), the two tissues were not well-separated. Fig. 8e shows 2D histograms for the whole volume (left) and the segmented regions containing only

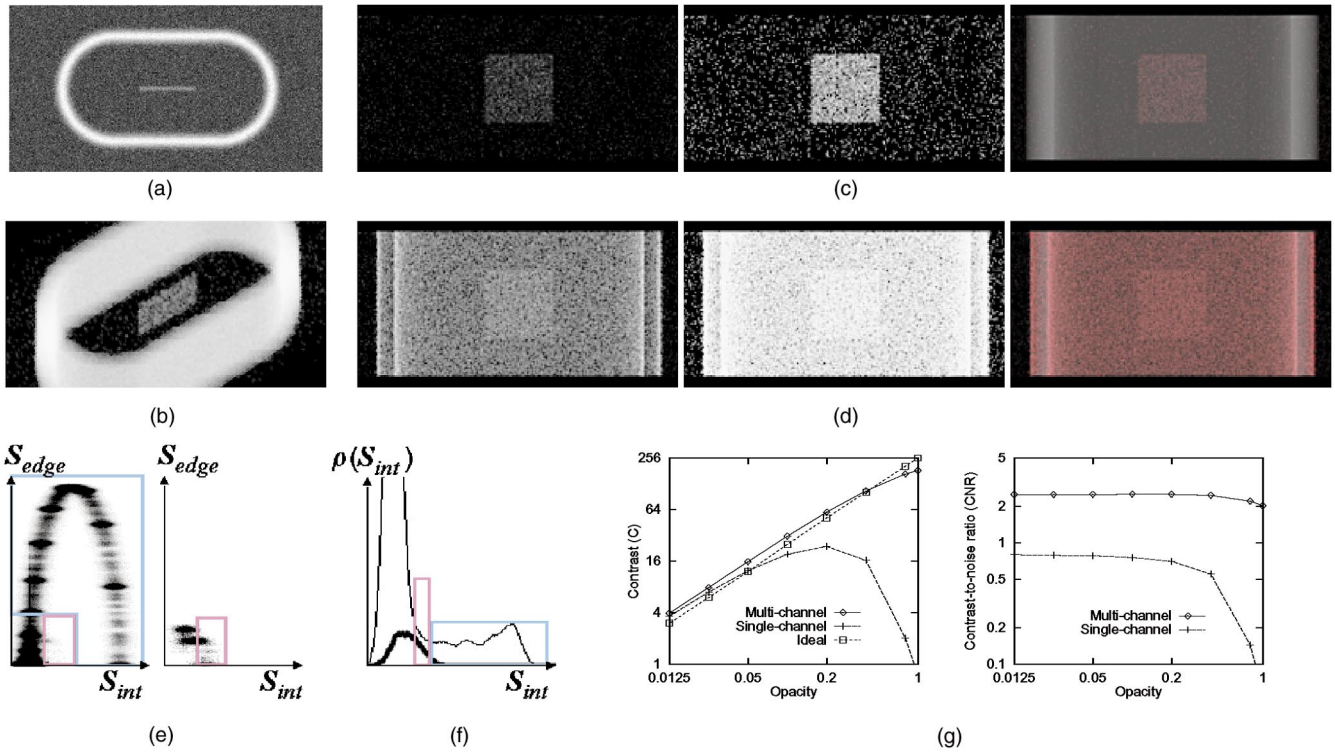

Fig. 8. Simulation for avoiding misclassification due to partial voluming (Guideline 1). (a) Cross section of synthesized volume. (b) Volume-rendered (VR) image of synthesized volume viewed from an oblique direction. (c) (Classification with 3D local structure) VR images of medium-intensity tissues using multichannel classification with low (0.1) and high (0.4) opacity values (left and middle) and color rendering of the medium (pink) and high (white) intensity tissues (right). (d) (Classification with original intensity) VR images of the medium-intensity region using single-channel classification with low (0.1) and high (0.4) opacity values (left and middle) and color rendering (right). (e) 2D histograms $\rho(\mathcal{S}_{int}, \mathcal{S}_{edge})$ for whole volume (left) and subvolume including only medium-intensity tissues (right) with opacity functions used for multichannel classification. Each opacity function had a constant value in the domain shown in the histograms with pink lines for medium-intensity and light-blue lines for high-intensity tissues. (In all the VR images in this paper, the opacity function had a constant value in the domain indicated in the histogram.) The opacity values for the color renderings were 0.1 (medium) and 0.01 (high) for the pink and light-blue domain, respectively. (f) 1D histograms $\rho(\mathcal{S}_{int})$ for whole volume (thin) and medium-intensity subvolume (bold) with opacity functions for single-channel classification. The subvolume histogram was amplified so that it could be compared with the whole volume one. (In all the subvolume histograms shown in this paper, similar amplification was performed.) The opacity functions had the same contant values as for multichannel classification in the interval shown in the histogram. (g) Plots of contrast C (left) and contrast-to-noise CNR (right) with variable opacity. In the ideal case, CNR should be infinity for every opacity value.

the target tissue (right). In the histogram for the whole image, an arch-shaped distribution corresponding to the "high" intensity tissue was observed and, thus, the target tissue "medium" could be effectively classified using Guideline 1. Fig. 8f shows 1D histograms of $\mathcal{S}_{int}$, which indicate that single-channel classification of the target tissue was inherently difficult due to unwanted intermediate intensities. The opacity functions are shown with the histograms.

We quantitatively evaluated our multichannel classification method. Because our aim was to enhance the visualization of target tissues, measures that would demonstrate the quality of the resultant rendered images were used as the evaluation criteria rather than measures of classification accuracy. For this purpose, we used the contrast C between the target tissue and background, and the contrast-to-noise ratio CNR [27]. We chose the definitions of C and CNR given by

$$C = I_t - I_b \tag{33}$$

and

$$CNR = \frac{I_t - I_b}{(h_t\sigma_t^2 + h_b\sigma_b^2)^{\frac{1}{2}}}, \tag{34}$$

where I_t, σ_t^2, and h_t, and I_b, σ_b^2, and h_b are the average intensity, variance, and number of pixels of the target tissue region and of the background in a rendered image, respectively [27]. CNR, which represents a normalized tissue contrast that is invariant to linear transformation of intensity, is widely used to evaluate essential tissue contrast improvements in the visualization of medical data when contrast materials are used during data acquisition [28] or postprocessing methods are applied to acquired data [29]. Fig. 8g shows C (left) and CNR (right) plotted for the rendered images using both single- and multichannel classification. C was also plotted for an ideal rendered image generated from a volume comprised of only the target tissue without noise. It is empirically known that, in volume rendering, the contrast of target tissue is largely dependent on the opacity. Thus, we also evaluated the effect of opacity on C and CNR. Using single-channel classification, the contrast C was maximum when the opacity was 0.2 and became similar to the ideal case in the low-opacity range (≤ 0.05). Using multichannel classification, C was nearly equal to the ideal case, except in the

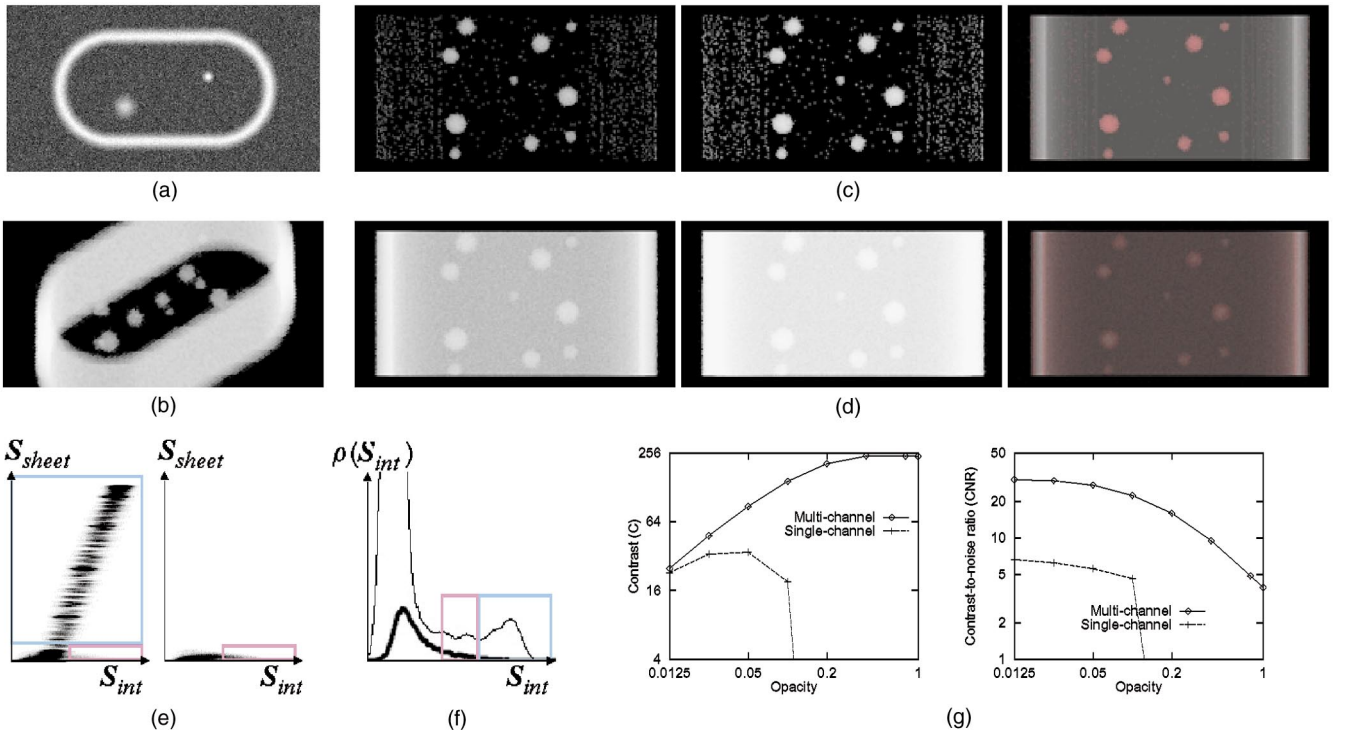

Fig. 9. Simulation of blob and sheet classification (Guideline 2). (a) Cross section of synthesized volume. (b) VR image of synthesized volume viewed from an oblique direction. (c) (Classification with 3D local structures) VR images of blobs using multichannel classification with low (0.05) and high (0.1) opacity values (left and middle) and color rendering of the blob (pink) and sheet (white) structures (right). (d) (Classification with original intensity) VR images of blobs using single-channel classification with low (0.05) and high (0.1) opacity values (left and middle) and color rendering (right). (e) 2D histograms $\rho(\mathcal{S}_{int}, \mathcal{S}_{sheet})$ for whole volume (left) and subvolumes including only blob tissues (right) with opacity functions for multichannel classification. The opacity values for the color rendering were 0.1 (blob) and 0.02 (sheet) in the pink and light-blue domains, respectively. (f) 1D histograms $\rho(\mathcal{S}_{int})$ for whole volume (thin) and blob subvolumes (bold) with opacity functions for single-channel classification. For monochrome rendering, the same opacity value was assigned to both the intervals shown by pink and light-blue lines to maximize the visibility of the blob tissues. For the color rendering, the opacity was 0.02 (blob) and 0.02 (sheet) for pink and light-blue intervals, respectively. (g) Plots of C (left) and CNR (right) with variable opacity.

large-opacity range (≥ 0.4), and decreased monotonically with the opacity. The contrast-to-noise ratio CNR significantly decreased at large opacity values using single-channel classification, but was much higher and almost constant using multichannel classification methods. In summary, using multichannel classification, the ideal contrast could be obtained over a wider range of opacity, and CNR was significantly high, which results in clear visualization with easy parameter adjustment. Using single-channel classification, the opacity needed to be sufficiently small to balance C and CNR, which results in vague visualization with difficult parameter adjustment.

5.1.2 Blob and Sheet Classification

We considered a situation where blobs were surrounded by a sheet structure and the intensity values of the two types of structure were similar. Blob and sheet structures can be regarded as representative of nodules and cortices, respectively. We modeled blobs of various sizes (which were 3D isotropic Gaussian functions variable in height and width [standard deviation], with an average height and standard deviation of 100 and 3.0, respectively) surrounded by the same sheet structure as that described in Section 5.1.1. Fig. 9a shows a cross section of the synthesized volume with random noise, while Fig. 9b depicts a volume-rendered image of the synthesized volume viewed from an oblique direction. The blobs were surrounded by an oval-shaped wall. The goal was to visualize the blobs (the target tissues) through the surrounding sheet structure.

Guideline 2 was utilized to classify the voxels into two tissue classes, $\mathbf{t} =$ ("sheet," "blob") using the feature vector $\mathbf{p} = (\mathcal{S}_{int}, \mathcal{S}_{sheet})$, where $\sigma_f = 4.0$ for $\mathcal{S}_{sheet}$. Fig. 9c and Fig. 9d show rendered images obtained using multi and single-channel classification, respectively. Using multichannel classification, the contrast of the blobs was sufficiently high since the effect of the overlapping sheet structure was mostly removed. Using single-channel classification, however, the blobs were only vaguely imaged due to unwanted sheet structure overlap, although the contrast could be improved by opacity adjustment. Fig. 9e shows the opacity functions with 2D histograms. In the histograms, the sheet structure is distributed along a diagonal (left) while the blob structures are distributed only in the area with very low $\mathcal{S}_{sheet}$ values (right). These histograms clarify the reason why the two structures could be effectively classified using Guideline 2. Fig. 9f shows 1D histograms for $\mathcal{S}_{int}$ which indicate the inherent difficulty of single-channel classification. Fig. 9g shows plots of C and CNR, which confirm the effectiveness of multichannel classification. Using single-channel classification, visualization of the blobs was possible only in the low-opacity range (≤ 0.1), resulting in insufficient contrast.

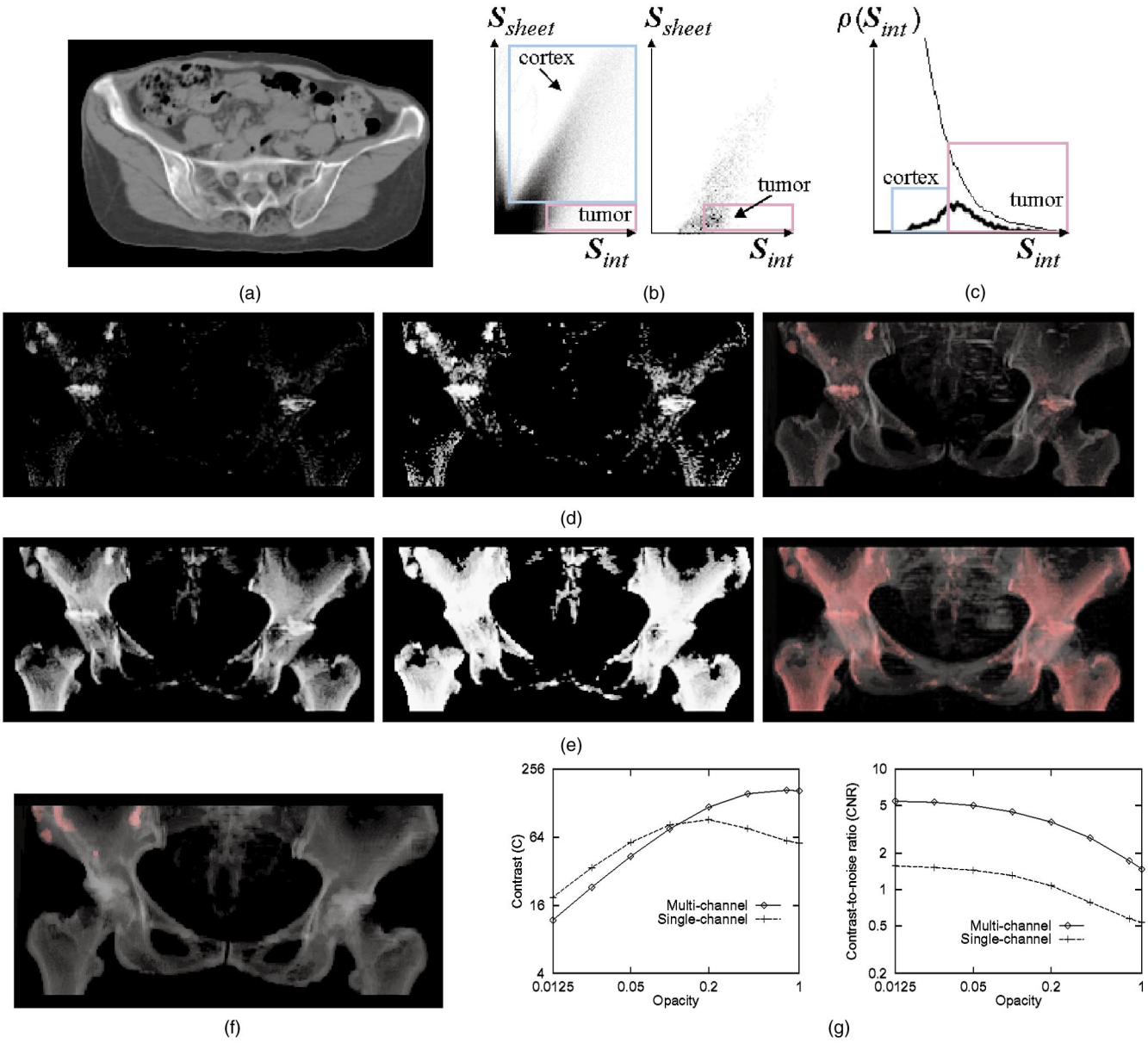

Fig. 10. Visualization of pelvic bone tumors from CT data. (a) Original CT image. (b) 2D histograms $\rho(\mathcal{S}_{int}, \mathcal{S}_{sheet})$ for whole volume (left) and manually traced tumor regions (right) with opacity functions for multichannel classification, where $\mathcal{S}_{int} \in [1000, 2200]$. The opacity functions for the tumors (pink lines) and bone cortex (light-blue lines) are shown. (c) 1D histograms $\rho(\mathcal{S}_{int})$ for whole volume (thin) and tumor regions (bold) with opacity functions for single-channel classification. (d) (Classification with 3D local structures) VR images of tumors using multichannel classification with low (0.1) and high (0.4) opacity values (left and middle) and color VR image (right) of tumors (pink, opacity 0.1) and bone cortices (white, opacity 0.02). (e) (Classification with original intensity) VR images of tumors using single-channel classification with two opacities (left and middle) and color rendering (right). The opacity values were 0.1 for tumors and 0.01 for bone cortex. (f) Color VR images of manually traced tumor regions. (g) Plots of C (left) and CNR (right) with variable opacity.

5.2 Medical Applications

We applied the proposed classification method to four different medical applications using volume data obtained with CT and MRI scanners. Each of the applications has a specific aim in areas such as diagnosis, medical research, or surgical planning. For these applications, different multichannel tissue classification strategies were designed using 3D local intensity structure filters. In Figs. 10, 11, 12, and 13, the (a) series of figures show an original CT or MR slice image, the (b) series show 2D histograms with the multichannel classification strategy and opacity functions, the (c) series show 1D histograms with conventional single-channel opacity functions (the height of 1D opacity functions are roughly related to their opacity values), and the (d) and (e) series show the results rendered with different opacity values using multi and single-channel classification, respectively.

5.2.1 *Visualization of Pelvic Bone Tumors*

Fig. 10 shows the results of bone tumor visualization from CT data of the pelvis. The aim was to visualize the distribution of bone tumors and localize them in relation

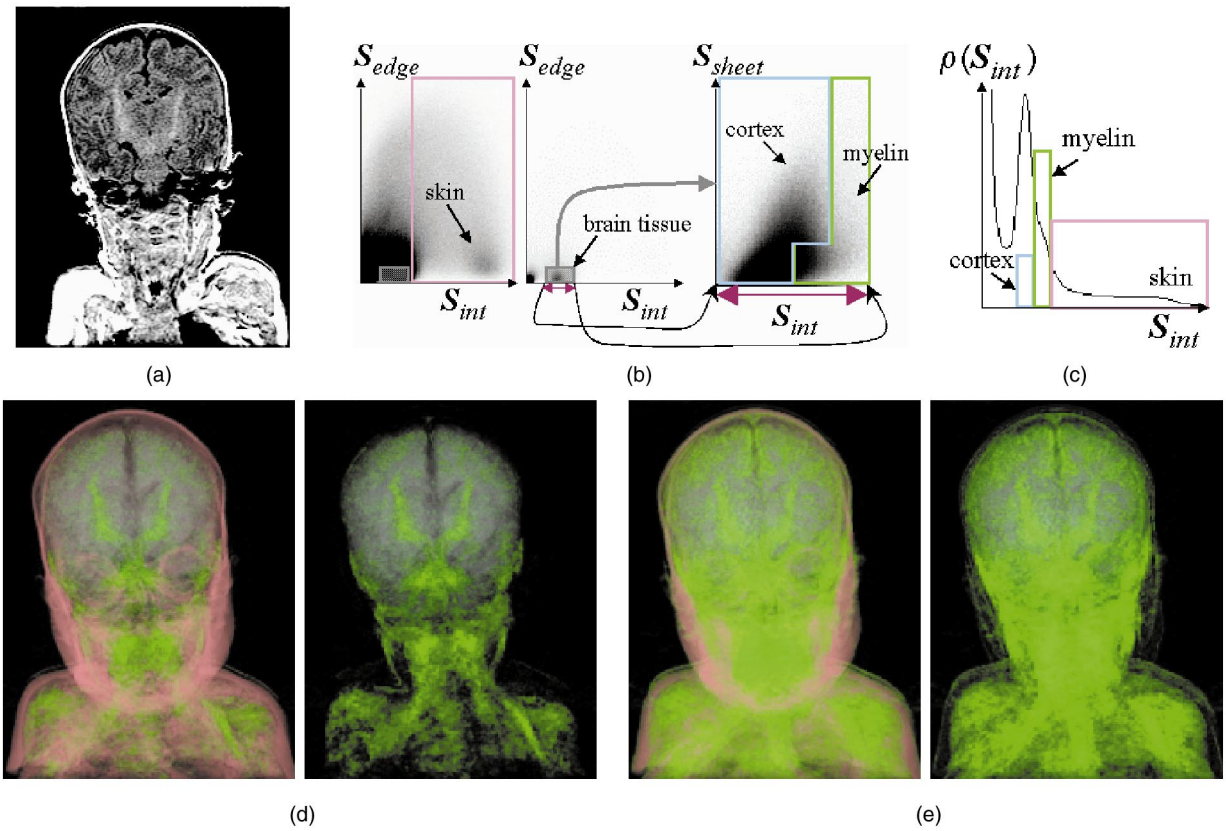

Fig. 11. Visualization of brain development process from MRI data. (a) Original MR image. (b) 2D histograms with classification strategy and opacity functions for multichannel classification. Left and middle: 2D histogram $\rho(\mathcal{S}_{int}, \mathcal{S}_{edge})$, where $\mathcal{S}_{int} \in [0, 360]$. Low density (left) and high density (middle) distributions are displayed with different density ranges. The opacity function for skin (pink lines) and discrete classification for brain tissues (shaded gray area) are shown. Right: 2D histogram $\rho(\mathcal{S}_{int}, \mathcal{S}_{sheet})$ for voxels classified as brain tissues, where $\mathcal{S}_{int} \in [50, 110]$. The opacity functions for the cortex (light-blue lines) and myelin (green lines) tissues are shown. (c) 1D histogram $\rho(\mathcal{S}_{int})$ with opacity functions for single-channel classification. (d) (Classification with 3D local structures) VR images of skin (pink), brain cortex (white), and myelin (green) using multichannel classification. Left: The opacity values were 0.02, 0.005, and 0.04 for skin, brain cortex, and myelin, respectively. Right: The opacity for skin was zero. (e) (Classification with original intensity) VR iamges using single-channel classification with the same opacity values as (d).

to the pelvic structure for biopsy planning, as well as diagnosis [30]. We used 40 CT slices with a 512 × 512 matrix (Fig. 10a). Both the slice thickness and reconstruction pitch were 5 mm. The original voxel dimensions were 0.82 × 0.82 × 5 (mm^3). After the matrix was reduced to half in the xy-plane, the volume data were interpolated along the z-axis using sinc interpolation so that the voxel was isotropic; its dimensions were then 1.64^3 (mm^3).

Healthy bone cortex tissues and bone tumors have similar original CT values. However, cortices are sheet-like in structure while tumors are not. The classification strategy was based on Guideline 2. We classified the voxels into two tissue classes $\mathbf{t} =$ ("cortex," "tumor") using the feature vector $\mathbf{p} = (\mathcal{S}_{int}, \mathcal{S}_{sheet})$, where $\sigma_f = 1.0$ for $\mathcal{S}_{sheet}$ (Fig. 10b). The right frame of Fig. 10b shows the 2D histogram for the manually traced tumor regions. It should be noted that the tumor regions were mainly distributed in the area with a relatively low $\mathcal{S}_{sheet}$ value.

In Fig. 10d and Fig. 10e, the left and middle frames depict rendered images of only the tumor component at two opacities. The right frames show the color renderings for both bone tumors and cortices. Fig. 10f shows the rendered color image generated from the tumor regions manually traced by a radiology specialist, which is regarded as an ideal visualization. The color rendering of Fig. 10d was well-correlated with that of Fig. 10f (the "ideal" image) and the bone tumors were visualized considerably better than in Fig. 10e. However, nontumor regions were also detected, mainly due to partial voluming of bone and articular space in Fig. 10d. Fig. 10g shows plots of C and CNR, which exhibit similar characteristics to those observed in Section 5.1 and confirm the usefulness of the proposed multichannel classification.

5.2.2 Visualization of the Brain Developmental Process

Fig. 11 shows the results of visualizing the brain developmental process of a newborn baby from MRI data. The aim was to visualize the brain developmental process called myelination, the process by which the myelin sheath is created in the subcortical brain, in relation to the skin and brain surfaces [31]. We used 124 MR image slices with a 256 × 256 matrix (Fig. 11a). The original voxel dimensions were 0.7 × 0.7 × 1.5 (mm^3). The data were interpolated along the z-axis using sinc interpolation so that the voxel was isotropic (0.7^3 mm^3).

Skin (and also subcutaneous fat) has higher intensity values than brain tissues, including the cortex and myelin. The skin and brain tissues were classified using Guideline 1. The left and middle frames of Fig. 11b show histogram $\rho(\mathcal{S}_{int}, \mathcal{S}_{edge})$ for the whole 3D image. Since the histogram

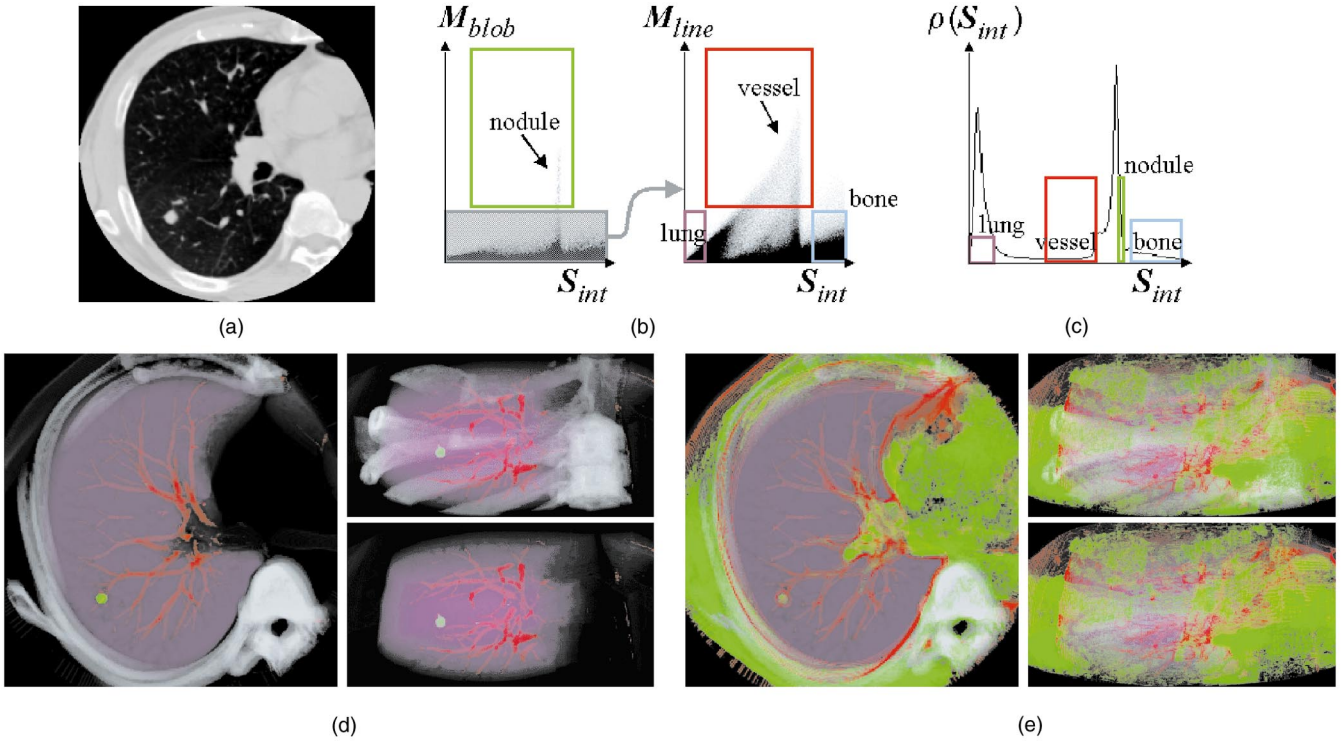

Fig. 12. Visualization of lung for computer-assisted diagnosis of cancer detection from CT data. (a) Original CT image. (b) 2D histograms with classification strategy and opacity functions for multichannel classification. Left: 2D histogram $\rho(\mathcal{S}_{int}, \mathcal{M}_{blob})$, where $\mathcal{S}_{int} \in [-1000, 500]$. The opacity function for the nodule (green lines) and discrete classification for the nonnodule tissues (shaded gray area) are shown. Right: 2D histogram $\rho(\mathcal{S}_{int}, \mathcal{M}_{line})$ for voxels classified as nonnodule tissues. The opacity functions for vessels (red lines), bone (light-blue lines), and lung (purple lines) are shown. (c) 1D histogram $\rho(\mathcal{S}_{int})$ with opacity functions for single-channel classification. (d) (Classification with 3D local structures) VR images of nodule (green), vessels (red), lung (purple), and bone (white) using multichannel classification. Left and upper right: The opacity values were 0.2, 0.1, 0.004, and 0.02 for nodule, vessles, lung, and bone, respectively. Top (left) and oblique (upper right) views are shown. Lower right: oblique view with zero opacity for bone. (e) (Classification with original intensity) VR images using single-channel classification with the same opacity values and view directions as (d) except that the nodule opacity was 0.1.

had a very wide dynamic range, low density (left) and high density (middle) distributions were displayed with different density ranges. In the left frame, an arch-shaped distribution can be observed, as was seen in the left frame of Fig. 8e. The main cluster of the skin regions is found around the bottom of the right arm of the arch (left). Brain tissues with low $\mathcal{S}_{edge}$ values (middle) were further classified into myelin and other tissues. While the intensity values of myelin were relatively high as compared with those of other brain tissues, they gradually changed and were similar to those of the brain cortex in the lower intensity region. However, brain cortices are sheet-like in structure, whereas myelin is not. Myelin was thus classified using Guideline 2 with the sheet filter in the ambiguous intensity range (the right frame of Fig. 11b). In summary, we classified the voxels into three tissue classes $\mathbf{t} =$ ("skin," "cortex," "myelin") using the feature vector $\mathbf{p} = (\mathcal{S}_{int}, \mathcal{S}_{edge}, \mathcal{S}_{sheet})$, where $\sigma_f = 1.0$ for $\mathcal{S}_{edge}$ and $\sigma_f = 1.0$ for $\mathcal{S}_{sheet}$. The strategy is summarized as follows:

$$\begin{aligned}
&\text{IF} \quad \mathcal{S}_{int} \text{ is high OR } \mathcal{S}_{edge} \text{ is high} \quad \text{THEN} \quad \Theta_{skin}(\mathbf{p}) = 1,\\
&\text{ELSE IF} \quad \mathcal{S}_{int} \text{ is high} \quad \text{OR}\\
&\qquad \mathcal{S}_{int} \text{ is intermediate AND } \mathcal{S}_{sheet} \text{ is low}\\
&\qquad\quad \text{THEN} \quad \Theta_{myelin}(\mathbf{p}) = 1,\\
&\text{ELSE} \quad \Theta_{cortex}(\mathbf{p}) = 1.
\end{aligned} \tag{35}$$

In Fig. 11d, the myelin tissues, which are V-shaped subcortical brain structures, were clearly depicted in relation to the skin and brain surfaces. Unwanted structures classified as myelin tissues appearing in Fig. 11e, which came from the boundaries of skin regions and brain cortices, were significantly reduced using multichannel classification.

5.2.3 *Visualization of the Lung for Computer-Assisted Diagnosis*

Fig. 12 shows the results of visualization of the lung from CT data aimed at computer-assisted diagnosis for the detection of early-stage lung cancers [32], [33], [34]. The goal was to visualize nodules in relation to the lung field, vessels, and ribs. We used 60 CT image slices with a 512 × 512 matrix (Fig. 12a). The slice thickness and reconstruction pitch were 2 mm and 1 mm, respectively. The matrix size of each slice was reduced to 256 × 256, after which the voxel dimensions were regarded as 0.78 × 0.78 × 1 (mm^3). The

data were then interpolated along the z-axis using sinc interpolation so that the voxel was isotropic.

While nodules, vessels, and other soft tissues have similar CT values in original images, the nodules and vessels have blob and line structures, respectively. The multiscale blob filter $\mathcal{M}_{blob}$ (Fig. 12b left) and the multiscale line filter $\mathcal{M}_{line}$ (Fig. 12b right) were used to detect the different widths of nodules and vessels according to Guideline 2. In both the histograms shown in Fig. 12b, the nodule and vessel components can be clearly observed. The lung field (mainly air) and bone have low and high CT values, respectively, in original images and they can be classified using the conventional method. In summary, we classified the voxels into four tissue classes $\mathbf{t} =$ ("nodule," "vessel," "lung," "bone") using the feature vector $\mathbf{p} = (\mathcal{S}_{int}, \mathcal{M}_{blob}, \mathcal{M}_{line})$, where $\sigma_1 = 2.0$, $s = \sqrt{2}$, and $n = 3$ in (19) for $\mathcal{M}_{blob}$, and $\sigma_1 = 1.0$, $s = \sqrt{2}$, and $n = 3$ for $\mathcal{M}_{line}$. The strategy is summarized as follows:

$$\begin{aligned} &\text{IF} \quad \mathcal{M}_{blob} \text{ is high} \quad \text{THEN} \quad \Theta_{nodule}(\mathbf{p}) = 1, \\ &\text{ELSE IF} \quad \mathcal{M}_{line} \text{ is high} \quad \text{THEN} \quad \Theta_{line}(\mathbf{p}) = 1, \\ &\text{ELSE} \quad \Theta_{lung}(\mathbf{p}) = 1, \quad \Theta_{bone}(\mathbf{p}) = 1. \end{aligned} \tag{36}$$

The nodules and vessels were clearly depicted with different colors using multichannel classification (Fig. 12d), while it was difficult to classify soft tissues into different categories using only intensity values (Fig. 12e).

5.2.4 Visualization of the Brain for Neurosurgical Planning

Fig. 13 shows the results of visualization of the brain from MR images. The visualization of brain vessels is particularly useful for surgical planning and navigation [35]. The aim was to visualize the relationships of the skin, brain surfaces, vessels, and a tumor. Because, in this case, the tumor was located near the ventricle, this also needed to be visualized. We used 80 MR image slices with a 256 $\times$ 256 matrix (Fig. 13a). The original voxel dimensions were 1.0 $\times$ 1.0 $\times$ 1.2 (mm^3). The data were interpolated along the z-axis using sinc interpolation so that the voxel was isotropic.

In the following, 3D local intensity structures were first employed to classify the skin, brain surfaces, and vessels. Next, the volume of interest (VOI) method was used to classify the tumor and ventricle. The two classifications were then combined to obtain final visualization.

In the histogram $\rho(\mathcal{S}_{int}, \mathcal{M}_{line})$ (Fig. 13b, left), the distribution can be seen to branch out in two distinct directions as $\mathcal{S}_{int}$ increases—a strong component along the $\mathcal{S}_{int}$ axis, which mainly corresponds to the skin cluster, and a relatively weak diagonal component, which mainly corresponds to the vessel cluster. Thus, vessels were classified using the $\mathcal{M}_{line}$ filter according to Guideline 2. Nonvessel tissues were further classified into skin and other tissues using Guideline 1 (Fig. 13b, middle). The brain was further differentiated from nonskin tissues, which include the brain and skull. Although the brain and skull had similar intensity values, the brain could be classified using the $\mathcal{S}_{sheet}$ filter with a relatively thick width (Guideline 2), which enhanced the skull tissue (Fig. 13b, right). The classification strategy for $\mathbf{t} =$ ("vessel," "skin," "brain") using $\mathbf{p} = (\mathcal{S}_{int}, \mathcal{S}_{edge}, \mathcal{M}_{line}, \mathcal{S}_{sheet})$ is summarized as:

$$\begin{aligned} &\text{IF} \quad \mathcal{M}_{line} \text{ is high} \quad \text{THEN} \quad \Theta_{vessel}(\mathbf{p}) = 1, \\ &\text{ELSE IF} \quad \mathcal{S}_{int} \text{ is high OR } \mathcal{S}_{edge} \text{ is high} \\ &\quad \text{THEN} \quad \Theta_{skin}(\mathbf{p}) = 1, \\ &\text{ELSE IF} \quad \mathcal{S}_{edge} \text{ is low AND } \mathcal{S}_{sheet} \text{ is low} \\ &\quad \text{THEN} \quad \Theta_{brain}(\mathbf{p}) = 1, \end{aligned} \tag{37}$$

where $\sigma_f = 1.0$ for $\mathcal{S}_{edge}$, $\sigma_1 = 1.0$, $s = \sqrt{2}$, $n = 3$ for $\mathcal{M}_{line}$, and $\sigma_f = 2.0$ for $\mathcal{S}_{sheet}$.

Using the single channel, it was quite difficult to discriminate skin and vessels since they had similar intensity distributions in the original intensity image (Fig. 13e). Also, unwanted structures corresponding to the skull were regarded as brain tissues. Using multichannel classification, the classification accuracy was significantly improved, although the helix of the ear and the rims of biopsy holes were misclassified as vessels (Fig. 13d). The color renderings using multichannel classification clearly depicted the three tissues of interest.

The tumor and brain ventricle were classified using the volume of interest (VOI) specified by the user. When a tissue of interest is sufficiently localized and has sufficient contrast compared with neighboring tissues, it can be classified using a VOI whose shape is relatively simple and easy to specify, for example, ellipsoidal or rectangular. Let $\mathcal{B}_{tumor}$ and $\mathcal{B}_{vent}$ be binary images whose pixel values are one within the VOI and zero otherwise, where the VOI has an ellipsoidal shape which includes the tumor and ventricle, respectively. The tumor is brighter than neighboring tissues and the ventricle is darker. Thus, the classification strategy using a VOI is given by

$$\begin{aligned} &\text{IF} \quad \mathcal{B}_{tumor} = 1 \text{ AND } \mathcal{S}_{int} \text{ is high} \quad \text{THEN} \quad \Theta_{tumor}(\mathbf{p}') = 1, \\ &\text{ELSE IF} \quad \mathcal{B}_{vent} = 1 \text{ AND } \mathcal{S}_{int} \text{ is low} \\ &\quad \text{THEN} \quad \Theta_{vent}(\mathbf{p}') = 1, \end{aligned} \tag{38}$$

where $\mathbf{p}' = (\mathcal{S}_{int}, \mathcal{B}_{tumor}, \mathcal{B}_{vent})$.

Fig. 13g shows a stereo pair of rendered images of the skin, brain, vessels, ventricle, and tumor resulting from the combination of the 3D local intensity structure and VOI classifications. To obtain the image depicted in Fig. 13g, strategy (38), whose opacity functions are shown in Fig. 13f, was first applied, after which strategy (37) was applied for the remaining voxels.

6 Discussion and Conclusions

We have described a novel approach to multichannel tissue classification of a scalar volume using 3D filters for the enhancement of specific local structures such as edge, sheet, line, and blob. Here, we discuss the work from several aspects and indicate the directions of future work.

6.1 Benefits of Local-Structure Enhancement Filtering Combined with Volume Rendering

One of the key criteria for evaluating visualization methods is the objectivity of rendered images. Although interactive segmentation processes steered by an operator, usually a physician or medical technician, are commonly involved in extracting tissues of interest, these processes, including

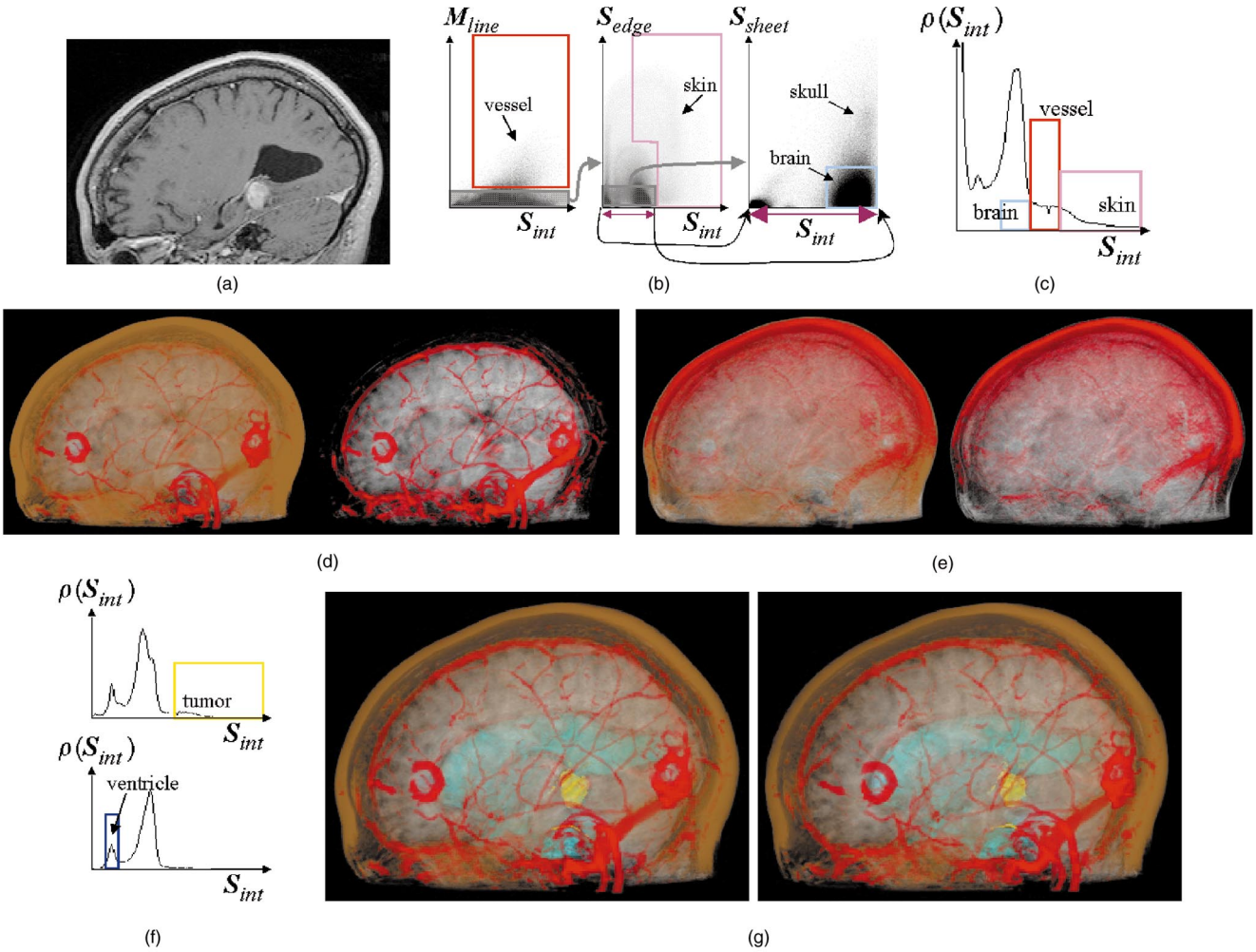

Fig. 13. Visualization of brain for neurosurgical planning from MRI data. (a) Original MRI image. (b) 2D histograms with classification strategy and opacity functions for multichannel classification. Left: 2D histogram $\rho(\mathcal{S}_{int}, \mathcal{M}_{line})$ ($\mathcal{S}_{int} \in [0, 450]$). The opacity function for vessel (red lines) and discrete classification for nonvessel tissues (shaded gray area) are shown. Middle: 2D histogram $\rho(\mathcal{S}_{int}, \mathcal{S}_{edge})$ for voxels classified as nonvessel tissues ($\mathcal{S}_{int} \in [0, 450]$). The opacity function for skin (pink lines) and discrete classification for nonskin tissues (shaded gray area) are shown. Right: 2D histogram $\rho(\mathcal{S}_{int}, \mathcal{S}_{sheet})$ for voxels classified as nonskin tissues ($\mathcal{S}_{int} \in [0, 180]$). The opacity function for brain is shown with light-blue lines. (c) 1D histogram $\rho(\mathcal{S}_{int})$ with opacity functions for single-channel classification. (d) (Classification with 3D local structures) VR images of skin (brown), brain (white), and vessels (red) using multichannel classification. Left: The opacity values were 0.1, 0.07, and 0.025 for vessels, skin, and brain, respectively. Right: The opacity for skin was zero. (e) (Classification with original intensity) VR images of skin, brain, and vessels using single-channel classification. Left: The opacity values were 0.05, 0.05, and 0.025 for vessels, skin, and brain, respectively. Right: The opacity for skin was zero. (f) 1D histograms within volumes of interest defined by $\mathcal{B}_{tumor}$ and $\mathcal{B}_{vent}$ with opacity functions for the tumor (upper) and ventricle (lower). (g) (Classification with 3D local structures and volumes of interest) VR images of skin, brain, vessel, tumor (yellow), and ventricle (cyan) resulting from combined multichannel classification using 3D local intensity structures and volumes of interest. The opacity values were 0.2, 0.03, 0.02, 0.4, and 0.05 for vessels, skin, brain, tumor, and ventricle, respectively. A stereoscopic view can be obtained using the cross-eye method.

manual editing, not only increase the operator's burden, but also make rendered images operator-dependent, that is, lacking in objectivity. For example, in a task such as that depicted in Fig. 10 (bone tumor visualization), not only is it necessary for the radiologist to spend considerable time interactively segmenting out all the tumor regions, even then it is very easy for some of them to be overlooked. In our proposed multichannel classification, tissues of interest are characterized by explicitly defined classification rules based on 3D local structure filters whose characteristics are well-understood. Thus, more objective classification is realized.

One problem in volume rendering is the difficulty of adjusting opacity functions. In our multichannel classification, parameter tuning is needed for the filtered responses, as well as for the original intensity. This means that the operator's burden is superficially increased. However, as demonstrated in Section 5, 2D histograms used in multichannel classification tend to exhibit more distinctly separated clusters corresponding to tissues of interest even when their clusters cannot be segregated in a 1D histogram. In practice, therefore, 2D histograms, which are essentially 2D projections of an m-dimensional histogram (m being the number of features), guide the operator in properly adjusting the opacity function parameters once the classification strategy has been designed. Thus, the operator's burden is essentially reduced while the quality of rendered images is significantly improved.

In summary, while a combination of perfect segmentation and surface rendering provides clear-cut visualization,

it suffers from the risk of fatal overlook, operator-dependence, and operator's burden. Our approach, that is, a combination of enhancement filtering and volume rendering with opacity adjustment, provides more objective visualization and greatly reduces the operator's burden.

The following future work is envisaged: First, semiautomated optimization of opacity functions should be investigated. As our method now stands, opacity function parameter tuning is manually performed and is not based on mathematical criteria. We consider that such criteria will be obtainable by analyzing 2D histograms of whole and sampled data (as shown in Fig. 10b). However, the sampled data should not be acquired by time-consuming manual tracing. We are now building an interactive system for opacity function optimization based on whole and sampled data acquired by specifying a tissue of interest using a simple VOI shape. Second, the utility of 3D local structures should be evaluated from the clinical point of view. Each of the medical problems referred to in Section 5.2 is clinically important. We believe that clinical validation of our method, using a large set of volume data for each specific medical area, is an important aspect of future work.

6.2 Effect of Anisotropic Voxels

Our 3D local structure filtering methods assume the isotropy of voxels in the input volume data. While we use sinc interpolation preprocessing in the third (z-axis) direction to make voxels isotropic, such preprocessed data are inherently blurrier in the third direction. The effect of anisotropic blurring on 3D filtering depends on the directions of local structures. For example, sheet (line) structures with narrow widths easily collapse when sheet normal (line) directions are close to (deviate from) the third direction. Three-dimensional local structure filtering would not be so effective in these cases. In recent work related to this problem, the effect of anisotropic voxels on the width quantification of sheet structures and its dependence on sheet normal directions were investigated in [36]. The results showed that anisotropy has a considerable effect on quantification accuracy. In the near future, however, the acquisition of volume data with (quasi-)isotropic voxels is expected to become much more common because of recent advances in CT and MR scanner technology in terms of high speed and resolution, such as multislice CT scanners [37], which means the problem of anisotropic voxels will become much less troublesome.

6.3 Design of a Classification Strategy

We have demonstrated classification strategies based on two guidelines: an edge filter for removing partial voluming by suppressing the edge structure and second-order local structure filters for highlighting or suppressing sheet, line, or blob structures. These local structures were combined with the original intensity to define a multidimensional feature space. The classification strategies were designed based on an interactive analysis of the local intensity structure of each tissue class following the two suggested guidelines. Although the processes for strategy design described in Section 4.2 are relatively straightforward, in practice they often involve trial and error because the criteria for filter selection are somewhat intuitive and the resultant classification strategy is not guaranteed to be optimal. Future work should therefore include the development of an automated method of ascertaining the optimal strategy, which will involve optimal filter type selection, as well as parameter adjustment. One way to accomplish it is to use traditional pattern classification methods based on multidimensional feature space analysis. Another possible approach would be to use an expert system which constructs an optimal strategy from examples of target (positive) and unwanted (negative) tissues [38], [39].

APPENDIX A

DERIVATION OF WIDTH RESPONSE CURVES FOR SECOND-ORDER STRUCTURES

The normalized response of the sheet filter to the sheet model, $\mathcal{S}_{sheet}\{h_{sheet}(\mathbf{x},\sigma_r);\sigma_f\}$, is written as

$$\mathcal{S}_{sheet}\{h_{sheet}(\mathbf{x},\sigma_r);\sigma_f\} = \beta\cdot\left\{-\frac{d^2}{dx^2}G(x;\sigma_f)\right\} * h_{sheet}(\mathbf{x},\sigma_r), \tag{39}$$

where β is the normalization factor. The width response curve for the sheet structure is defined by $\mathcal{S}_{sheet}\{h_{sheet}(\mathbf{0},\sigma_r);\sigma_f\}$, where $\mathbf{0}=(0,0,0)$.

The sheet structure with variable width σ_r is modeled by

$$\begin{aligned} h_{sheet}(\mathbf{x},\sigma_r) &= \exp\left(-\frac{x^2}{2\sigma_r^2}\right) \\ &= \sqrt{2\pi}\sigma_r G(x;\sigma_r), \end{aligned} \tag{40}$$

where $G(x;\sigma_r)$ is the 1D Gaussian function. By combining (39) and (40), we have:

$$\begin{aligned} &\mathcal{S}_{sheet}\{h_{sheet}(\mathbf{x},\sigma_r);\sigma_f\} \\ &= \beta\cdot\sqrt{2\pi}\sigma_r\left\{-\frac{d^2}{dx^2}G(x;\sigma_f) * G(x;\sigma_r)\right\} \end{aligned} \tag{41}$$

$$= \beta\cdot\sqrt{2\pi}\sigma_r\left\{-\frac{\partial^2}{\partial x^2}G\left(x;\sqrt{\sigma_f^2+\sigma_r^2}\right)\right\}, \tag{42}$$

in which we used the relation

$$G(x;\sigma_1) * G(x;\sigma_2) = G(x;\sqrt{\sigma_1^2+\sigma_2^2}).$$

Since

$$\frac{d^2}{dx^2}G(x;\sigma) = \left\{\left(\frac{x^2}{\sqrt{2\pi}\sigma^5}-\frac{1}{\sqrt{2\pi}\sigma^3}\right)\exp\left(-\frac{x^2}{2\sigma^2}\right)\right\}, \tag{43}$$

the width response curve for the sheet is given by

$$\begin{aligned} \mathcal{S}_{sheet}\{h_{sheet}(\mathbf{0},\sigma_r);\sigma_f\} &= \frac{\beta\sigma_r}{\left(\sqrt{\sigma_f^2+\sigma_r^2}\right)^3} \\ &= \frac{\beta}{\sigma_f^2}\cdot\frac{\left(\frac{\sigma_f}{\sigma_r}\right)^2}{\left(\sqrt{\left(\frac{\sigma_f}{\sigma_r}\right)^2+1}\right)^3}. \end{aligned} \tag{44}$$

Thus, $\mathcal{S}_{sheet}\{h_{sheet}(0,\sigma_r);\sigma_f\}$ is essentially a function of $\frac{\sigma_f}{\sigma_r}$ when $\beta=\sigma_f^2$, and its maximum is $\frac{2}{(\sqrt{3})^3}(\approx 0.385)$ when $\frac{\sigma_f}{\sigma_r}=\sqrt{2}$.

Using similar derivations, when the normalization factor $\beta=\sigma_f^2$ is multiplied, the width response curve for the line is given by

$$\mathcal{S}_{line}\{h_{line}(\mathbf{0},\sigma_r);\sigma_f\}=\frac{\sigma_f^2\sigma_r^2}{\left(\sqrt{\sigma_f^2+\sigma_r^2}\right)^4}=\frac{\left(\frac{\sigma_f}{\sigma_r}\right)^2}{\left(\sqrt{\left(\frac{\sigma_f}{\sigma_r}\right)^2+1}\right)^4}, \tag{45}$$

whose maximum is $\frac{1}{4}(=0.25)$ when $\frac{\sigma_f}{\sigma_r}=1$.

The width response curve for the blob is given by

$$\mathcal{S}_{blob}\{h_{blob}(\mathbf{0},\sigma_r);\sigma_f\}=\frac{\sigma_f^2\sigma_r^3}{\left(\sqrt{\sigma_f^2+\sigma_r^2}\right)^5}=\frac{\left(\frac{\sigma_f}{\sigma_r}\right)^2}{\left(\sqrt{\left(\frac{\sigma_f}{\sigma_r}\right)^2+1}\right)^5}, \tag{46}$$

whose maximum is $\frac{2}{3}(\sqrt{\frac{3}{5}})^5(\approx 0.186)$ when $\frac{\sigma_f}{\sigma_r}=\sqrt{\frac{2}{3}}$.

Appendix B

Sinc Interpolation without Gibbs Ringing

The sinc interpolation along the third (z-axis) direction is performed by zero-filled expansion in the frequency domain [22], [23]. Let $f(i)$ $(i=0,1,\ldots,n-1)$ be the profile in the third direction. In the discrete Fourier transform of $f(i)$, $f(i)$ should be regarded as cyclic and then $f(n-1)$ and $f(0)$ are essentially adjacent. Unwanted Gibbs ringing occurs in the interpolated profile due to the discontinuity between $f(n-1)$ and $f(0)$. Thus, Gaussian-shaped slopes were added at the beginning and end of $f(i)$ to avoid the occurence of unwanted ringing before the sinc interpolation. Let $f'(i)$ $(i=-3\cdot\sigma,\ldots,0,1,\ldots,n-1,n,\ldots,3\cdot\sigma+n)$ be the modified profile, which is given by

$$f'(i)=\begin{cases} G(i;\sigma)\cdot f(0), & i=-3\cdot\sigma,\ldots,0 \\ f(i), & i=0,\ldots,n-1 \\ G(i-n+1;\sigma)\cdot f(n-1), & i=n,\ldots,3\cdot\sigma, \end{cases} \tag{47}$$

where $G(x;\sigma)$ is the Gaussian function and the variation is sufficiently smooth everywhere, including between $f(3\cdot\sigma+n)$ and $f(-3\cdot\sigma)$. The discrete Fourier transform of $f'(i)$ was performed (we used $\sigma=4$). After the sinc interpolation of $f'(i)$, the added Gaussian-shaped slopes were removed.

Acknowledgments

This work was partly supported by U.S. National Insitutes of Health grant P01 CA67165-02 and JSPS Grant-in-Aid for Scientific Research (C)(2) 11680389. The authors would like to thank Dr. Gary Zientara and Dr. Petra Huppi of Harvard Medical School and Brigham and Women's Hospital for providing MR images of a baby's brain, Dr. Hironobu Ohmatsu of the National Cancer Center, Japan, for providing CT images of a chest, and Dr. Don Johann of New York University Medical School for providing MR images of a brain for neurosurgical planning. Yoshinobu Sato would also like to thank Dr. Hideki Atsumi and Dr. Nobuhiko Hata for helping him adapt to the environment of the Surgical Planning Laboratory at Harvard Medical School and Brigham and Women's Hospital and Prof. Ferenc Jolesz of Harvard Medical School for continuous encouragement. The work described in this paper was partly conducted while Yoshinobu Sato was a visiting research at the Surgical Planning Laboratory, Department of Radiology, Harvard Medical School and Brigham and Women's Hospital.

References

[1] M. Levoy, "Volume Rendering: Display of Surfaces from Volume Data," *IEEE Computer Graphics and Applications,* pp. 29-36, 1988.

[2] R.A. Drebin, L. Carpenter, and P. Hanrahan, "Volume Rendering," *Computer Graphics (Proc. SIGGRAPH '88),* vol. 22, pp. 65-73, 1988.

[3] G.D. Rubin, C.F. Beullieu, V. Anngiro, H. Ringle, A.M. Norbash, J.F. Feller, M.D. Dake, R.B. Jefferey, and S. Naple, "Perspective Volume Rendering of CT and MR Images: Applications for Endoscopic Imaging," *Radiology,* vol. 199, no. 2, pp. 321-330, 1996.

[4] P.T. Johnson, D.G. Heath, B.S. Kuszyk, and E.K. Fishman, "CT Angiography with Volume Rendering: Advantages and Applications in Splanchnic Vascular Imaging," *Radiology,* vol. 200, no. 2, pp. 564-568, 1996.

[5] C. Barillot, "Surface and Volume Rendering Techniques to Display 3-D Data," *IEEE Eng. in Medicine and Biology,* vol. 12, pp. 111-119, 1993.

[6] M.W. Vannier, R.L. Butterfield, D. Jordon, W.A. Murphy, R.G. Levitt, and M. Gado, "Multispectral Analysis of Magnetic Resonance Images," *Radiology,* vol. 154, no. 1, pp. 221-224, 1985.

[7] M.C. Clark, L.O. Hall, D.B. Goldgof, L.P. Clarke, R.P. Velthuizen, and M.S. Silbiger, "MRI Segmentation Using Fuzzy Clustering Techniques," *IEEE Eng. in Medicine and Biology,* vol. 13, pp. 730-742, 1994.

[8] Y. Sato, C.-F. Westin, A. Bhalerao, S. Nakajima, N. Shiraga, S. Yoshida, and R. Kikinis, "Tissue Classification Based on 3D Local Intensity Structures for Volume Rendering," *Proc. Japanese Associ. Medical Imaging Technology Frontier '97,* pp. 167-172. 1997. (Mpeg movies are available at http://www.image.med.osaka-u.ac.jp/~yoshi/vr_index.html).

[9] Y. Sato, S. Nakajima, H. Atsumi, T. Koller, G. Gerig, S. Yoshida, and R. Kikinis, "3D Multiscale Line Filter for Segmentation and Visualization of Curvilinear Structures in Medical Images," *Proc. Joint Conf. Computer Vision, Virtual Reality, and Robotics in Medicine and Medical Robotics and Computer-Assisted Surgery '97,* pp. 213-222, 1997.

[10] Y. Sato, S. Nakajima, N. Shiraga, H. Atsumi, S. Yoshida, T. Koller, G. Gerig, and R. Kikinis, "Three-Dimensional Multiscale Line Filter for Segmentation and Visualization of Curvilinear Structures in Medical Images," *Medical Image Analysis,* vol. 2, no. 2, pp. 143-168, 1998.

[11] H. Knutsson, "Representing Local Structure Using Tensors," *Proc. Sixth Scandinavian Conf. Image Analysis,* pp. 244-251, 1989.

[12] C.-F. Westin, "A Tensor Framework for Multidimensional Signal Processing," thesis no. 348, Linköping Univ., Sweden, 1994.

[13] T.M. Koller, G. Gerig, G. Szekely, and D. Dettwiler, "Multiscale Detection of Curvilinear Structures in 2-D and 3-D Image Data," *Proc. Fifth Int'l Conf. Computer Vision (ICCV '95),* pp. 864-869, 1995.

[14] G. Kindlmann and J. Durkin, "Semi-Automatic Generation of Transfer Functions for Direct Volume Rendering," *Proc. IEEE Symp. Volume Visualization,* pp. 79-86, 1998.

[15] D.H. Laidlaw, K.W. Fleischer, and A.H. Barr, "Partial-Volume Bayesian Classification of Material Mixtures in MR Volume Data Using Voxel Histograms," *IEEE Trans. Medical Imaging,* vol. 17, no. 1, pp. 74-86, 1998.

[16] R.M. Haralick, L.T. Watson, and T.J. Laffey, "The Topographic Primal Sketch," *Int'l J. Robotic Research,* vol. 2, pp. 50-72, 1983.

[17] C.-F. Westin, S. Warfield, A. Bhalerao, L. Mui, J. Richolt, and R. Kikinis, "Tensor Controlled Local Structure Enhancement of CT Images for Bone Segmentation," *Proc. Int'l Conf. Medical Image Computing and Computer-Assisted Intervention '98,* pp. 1,205-1,212, 1998.

[18] S. Yamamoto, M. Matsumoto, Y. Tateno, T. Iinuma, and T. Matsumoto, "Quoit Filter: A New filter Based on Mathematical Morphology to Extract the Isolated Shadow, and Its Application to Automatic Detection of Lung Cancer in X-Ray CT," *Proc. 13th Int'l Conf. Pattern Recognition (ICPR '96),* vol. 2, pp. 3-7, 1996.

[19] D. Marr, *Vision—A Computational Investigation into the Human Representation and Processing of Visual Information.* New York: W.H. Freeman, 1982.

[20] T. Lindeberg, "On Scale Selection for Differential Operators," *Proc. Eighth Scandinavian Conf. Image Analysis,* pp. 857-866, 1993.

[21] T. Lindeberg, "Edge Detection and Ridge Detection with Automatic Scale Selection," *Proc. IEEE Conf. Computer Vision and Pattern Recognition (CVPR '96),* pp. 465-470, 1996.

[22] N.M. Hylton, I. Simovsky, A.J. Li, and J.D. Hale, "Impact of Section Doubling on MR Angiography," *Radiology* vol. 185, no. 3, pp. 899-902, 1992.

[23] Y.P. Du, D.L. Parker, W.L. Davis, and G. Cao, "Reduction of Partial-Volume Artifacts with Zero-Filled Interpolation in Three-Dimensional MR Angiography," *J. Magnetic Resonance Imaging* vol. 4, no. 5, pp. 733-741, 1995.

[24] A. Kandel and S.C. Lee, *Fuzzy Switching and Automata.* New York: Crane Russak, 1979.

[25] W. Schroeder, K. Martin, and B. Lorensen, *The Visualization Toolkit: An Object-Oriented Approach to 3D Graphics,* second ed. Upper Saddle River, N.J.: Prentice Hall, 1998 (the visualization toolkit, at http://www.kitware.com/vtk.html).

[26] P. Lacroute and M. Levoy, "Fast Volume Rendering Using a Shear-Warp Factorization of the Viewing Transform," *Computer Graphics (Proc. SIGGRAPH '94),* vol. 28, pp. 451-458, 1994 (the VolPack volume rendering library, at http://www-graphics.stanford.edu/software/volpack).

[27] D.G. Brown and S.J. Riederer, "Contrast to-Noise Ratios in Maximum Intensity Projection Images," *Magnetic Resonance in Medicine,* vol. 23, no. 1, pp. 130-137, 1992.

[28] H.C. Schwickert, T.P. Roberts, A. Muhler, M. Stiskal, F. Demsar, and R.C. Brasch, "Angiographic Properties of Gd-DTPA-24-Cascade-Polymer—A New Macromolecular MR Contrast Agent," *European J. Radiology,* vol. 20, no. 2, pp. 144-150, 1995.

[29] K.Y. Ho, M.W. de Haan, A.G. Kessels, P.J. Kitslaar, and J.M. van Engelshoven, "Peripheral Vascular Tree Stenoses: Detection with Subtracted and Nonsubtracted MR Angiography," *Radiology,* vol. 206, no. 3, pp. 673-681, 1998.

[30] N. Shiraga, Y. Sato, E. Kohda, Y. Okada, K. Sato, T. Hasebe, K. Hiramatsu, R. Kikinis, and F.A. Jolesz, "Three Dimensional Display of the Osteosclerotic Lesion by Volume Rendering Method," *Nippon Acta Radiologica,* vol. 58, no. 2, p. S84, 1998.

[31] P.S. Huppi, S. Warfield, R. Kikinis, P.D. Barnes, G.P. Zientara, F.A. Jolesz, M.K. Tsuji, and J.J. Volpe, "Quantitative Magnetic Resonance Imaging of Brain Development in Premature and Mature Newborns," *Annals Neurology,* vol. 43, no. 2, pp. 224-235, 1998.

[32] A. Shimizu, J. Hasegawa, and J. Toriwaki, "Minimum Directional Difference Filter for Extraction of Circumscribed Shadows in Chest X-Ray Images and Its Characteristics," *IEICE Trans.,* vol. J-76D-II, no. 2, pp. 241-249. 1993.

[33] M.L. Giger, K.T. Bae, and H. MacMahon, "Computerized Detection of Pulmonary Nodules in Computed Tomography Images," *Investigative Radiology,* vol. 24, no. 4, pp. 459-465, 1994.

[34] K. Kanazawa, M. Kubo, N. Niki, H. Satoh, H. Ohmatsu, K. Eguchi, and N. Moriyama, "Computer Aided Screening System for Lung Cancer Based on Helical CT Images," *Proc. Visualization in Biomedical Computing,* pp. 223-228, 1996.

[35] S. Nakajima, H. Atsumi, R. Kikinis, T.M. Moriarty, D.C. Metcalf, F.A. Jolesz, and P.M. Black, "Use of Cortical Surface Vessel Registration for Image-Guided Neurosurgery," *Neurosurgery,* vol. 40, no. 6, pp. 1,201-1,210, 1997.

[36] Y. Sato, T. Kubota, K. Nakanishi, N. Sugano, T. Nishii, K. Ohzono, H. Nakamura, O. Ochi, and S. Tamura, "Three-Dimensional Reconstruction and Quantification of Hip Joint Cartilages from Magnetic Resonance Images," *Proc. Int'l Conf. Medical Image Computing and Computer-Assisted Intervention '99,* pp. 338-347, 1999.

[37] H. Hu, "Multi-Slice Helical CT: Scan and Reconstruction," *Medical Physics,* vol. 26, no. 1, pp. 5-18, 1999.

[38] J. Hasegawa and J. Toriwaki, "Automated Construction of Image Processing Procedures Based on Positive and Negative Sample Figures," *Proc. Asian Conf. Computer Vision '93 (ACCV '93),* pp. 573-578, 1993.

[39] A. Shimizu, X. Zhou, J. Hasegawa, and J. Toriwaki, "Automated Construction of Three Dimensional Image Processing Procedures by Pictorial Example," *Proc. 18th Int'l Conf. IEEE Eng. in Medicine and Biology Society (EMBS '96),* no. 682, 1996.

Yoshinobu Sato received his BS, MS, and PhD degrees in information and computer sciences from Osaka University, Japan, in 1982, 1984, 1988 respectively. From 1988 to 1992, he was a research engineer at the NTT Human Interface Laboratories. In 1992, he joined the Division of Functional Diagnostic Imaging of Osaka University Medical School as a faculty member. From 1996 to 1997, he was a research fellow in the Surgical Planning Laboratory, Harvard Medical School and Brigham and Women's Hospital. He is currently an associate professor in the Graduate School of Medicine and Graduate School of Engineering Science at Osaka University, where he leads a group conducting research on 3D image analysis and surgical navigation systems in the Division of Functional Diagnostic Imaging. He is a member of the IEEE. For more information, see http://www.image.med.osaka-u.ac.jp/~yoshi.

Carl-Fredrik Westin received his MSc degree in physics and electrical engineering in 1988, and the LicTechn degree on the topic "feature extraction from a tensor image descriptions" in 1991, from Linköping University, Sweden. In 1994, Westin received his PhD degree in computer vision. His thesis "A Tensor Framework for Multidimensional Signal Processing" presents a novel method for filtering uncertain and irregularly sampled data termed normalized convolution. Since 1996, Dr. Westin has been at Harvard Medical School, Brigham and Women's Hospital, Boston. His research interests are focused on medical applications of computer vision. He is currently working on automated segmentation of MRI and CT data using multidimensional signal processing techniques and level set methods. He is a member of the IEEE.

Abhir Bhalerao received a BSc degree in computer systems engineering in 1986 from the University of Warwick, United Kingdom. He worked as a programmer with a software-systems company (now EDS-Scicon) for two years being involved in real-time simulations software, e.g., graphical, networked systems for air traffic control training. Between 1988-1991, he was a researcher at the Image and Signal Processing group back at Warwick Computer Science, where he completed his PhD in image processing. He worked for an electronics company (Crosfield Electronics) for two years as an analyst programmer and was involved in a number of projects developing low-level software for communications systems used by the publishing industry. In 1993, he joined the Image Processing Group at Guy's and St. Thomas' Hospital, London, as part of the Advanced Medical Imaging project, sponsored by the hospital's Special Trustees. From February 1996-August 1997, he was a research fellow with the Surgical Planning Laboratory, Brigham and Women's Hospital, Harvard Medical School, Boston, working on segmentation methods for MR angiography data, volume rendering for surgical planning, and artifact correction in MRA. He returned as a lecturer to the University of Warwick in August 1998. His research interests are in medical image processing and computer vision.

Shin Nakajima received his MD in 1984 from Osaka University Medical School, Japan. He trained as a resident in the Department of Anesthesiology from 1984-1985 and in the Department of Neurosurgery at Osaka University Hospital. He worked for various hospitals until 1992 as a neurosurgeon. He became a board certified neurosurgeon in 1991. He was also a researcher in experimental cerebral ischemia. In 1993, he started working in the Department of Radiology and developing the Image Processing System for Neurosurgery at Osaka University Medical School. From July 1994-July 1997, he was a research fellow with the Surgical Planning Laboratory, Brigham and Women's Hospital, Harvard Medical School, Boston, working on image-guided neurosurgery, surgical simulation, and scalp localization for neurosurgery. In 1997, he returned to Japan and completed his PhD degree with the thesis "Use of Cortical Surface Vessel Registration for Image-Guided Neurosurgery." He is currently working as a neurosurgeon at Nakakawachi Center for Acute Medicine, Osaka, Japan. His research interests are in neurosurgical simulation and MR imaging for head injury.

Nobuyuki Shiraga graduated from Keio University School of Medicine and received his MD in 1986. He also took the board of Japanese Radiological Society 1992, after three years residency in the Department of Diagnostic Radiology, Keio University Hospital and training in the Department of Diagnostic Pathology for 13 months. From 1996 to 1997, he was a research fellow with the Surgical Planning Laboratory, Brigham and Women's Hospital, Harvard Medical School, Boston, working on diagnostic 3D images of bone tumors, as well as abdominal and vascular 3D images. He returned to Japan as an instructor in the Department of Diagnostic Radiology at Keio University School of Medicine in 1997. He is interested in diagnostic radiology generally, including 3D images.

Shinichi Tamura received his BS, MS, and PhD degrees in electrical engineering from Osaka University, Japan, in 1966, 1968, and 1971, respectively. He is currently a professor in the Medical School and the Graduate School of Engineering Science, Osaka University. He is an author/coauthor of more than 180 papers in scientific journals and has received several paper awards from journals/societies, including Pattern Recognition and Investigative Radiology. His current research activities include works in the field of image processing and its medical applications. Dr. Tamura is a member of the IEEE, the International Society for Computer Aided Surgery, the Institute of Electronics, Information and Communication Engineers of Japan, the Information Processing Society of Japan, the Japanese Society of Medical Imaging Technology, and the Japan Radiological Society. Currently, he is an associate editor of *Pattern Recognition* and a vice editor-in-chief of *Medical Imaging Technology*.

Ron Kikinis received his MD from the University of Zurich, Switzerland, in 1982. is the director of the Surgical Planning Laboratory of the Department of Radiology, Brigham and Women's Hospital and Harvard Medical School, Boston, and an associate professor of radiology at Harvard Medical School, as well as an adjoint professor of biomedical engineering at Boston University. His interests include the development of clinical applications for image processing, computer vision and interactive rendering methods. He is currently concentrating on developing fully automated segmentation methods and introducing computer graphics into the operating room. He is the author of 52 peer-reviewed articles.

Before joining Brigham and Women's Hospital in 1988, he worked as a researcher at the ETH in Zurich and as a resident at the University Hospital in Zurich, Switzerland. For more information, see http://www.spl.harvard.edu/pages/ppl/kikinis/cv.html.